Measurement of the τ Polarization using the VENUS detector at TRISTAN

A DISSERTATION

Presented in Partial Fulfillment of the Requirements
for the Degree of Doctor of Science
in the Graduate School of Osaka University

Hiroyuki Hanai

Osaka University

1996

Abstract

Polarization of τ leptons in the electron-positron annihilation process is measured using the e^+e^- collider, TRISTAN, at the center-of-mass energy of 58 GeV. The data used in this analysis were collected by the VENUS detector from 1991 to 1995 corresponding to the integrated luminosity of 271 pb^{-1}. From the kinematical distributions of the decay particles of τ lepton, the average polarization of τ lepton $\mathcal{P}_\tau$ and its forward-backward asymmetry $A_\mathcal{P}$ are measured to be 0.012 ± 0.058 and 0.029 ± 0.057, respectively. The present results are the significant improvements of the measurement in the energy region below Z^0 pole.

The measurement of $\mathcal{P}_\tau$ and $A_\mathcal{P}$ can be interpreted as the two vector coupling constants g_V^τ and g_V^e to be $g_V^\tau = -0.08 \pm 0.17$, $g_V^e = -0.03 \pm 0.07$. They are consistent with the Standard Model predictions and support the lepton universality.

Acknowledgement

This thesis work has been accomplished through efforts of many people. I wish to thank all the members of VENUS Collaboration, TRISTAN accelerator group and Nagashima group in Osaka University.

I would like to thank Prof. Y. Nagashima at first. He taught me many essential points in the research on high energy physics through many discussions and educated me how to study physics from a global point of view. Also he gave me an opportunity to take part in VENUS Collaboration.

I am deeply indebted to Dr. J. Haba for the completion of this thesis. I could not overcome many difficulties without his many helpful instructions and advice. Discussions with him were vital for the completion of this thesis.

I also thank Prof. T. Yamanaka and Dr. M. Takita for their helpful advice. I wish to thank them from my heart.

I wish to thank many collaborators in KEK. I would especially like to thank Dr. S. Odaka for his lucid discussions and useful suggestions from both experimental and theoretical points of view. My thanks go also to Prof. T. Matsui, Dr. M. Sakuda, Dr. S. Uehara, Dr. T. Tsuboyama, Dr. Y. Yamada and Dr. J. Kanzaki, who gave me a lot of advice.

I express my gratitude to my senior Dr. A. Suzuki, Dr. N. Kanda, Mr. F. Yabuki, and Dr. M. Miura, my colleagues Mr. T. Hara, Mr. D. Tatsumi, Mr. K. Yusa and Mr. K. Okabe for the useful discussions in my daily life. Also I wish to thank Mr. M. Yagi and other students in Nagashima group.

My special thank goes to Miss. S. Tsuzuki for her lots of kind supports.

Finally, I would also like to thank all the members of VENUS Collaboration and Nagashima group in Osaka University whom I have not mentioned above.

Contents

Chapter 1

Introduction

It has long been pointed[1] out that the polarization of τ leptons provides us with information concerning the neutral current properties of reaction

$$e^+e^- \to \tau^+\tau^- \tag{1.1}$$

as well as the cross section $R_{\tau\tau}$ and the charge asymmetry $A_{\tau\tau}$. They can be described by the electroweak theory which takes the most important role in the Standard Model[1]. Thus the experimental measurement of such observables can be used to test the Standard Model and constrains parameters used in the theory.

The coupling constants of electroweak interaction are some of many free parameters in the Standard Model. All the constants, in principle, can be derived from measurement of the total and the differential cross sections of two fermion final states in electron-positron annihilation experiments, although these measurements are not sensitive enough to measure the vector coupling constants.

On the other hand, the average polarization $\mathcal{P}_\tau$ and its forward-backward asymmetry $A_\mathcal{P}$ of τ leptons are sensitive to the vector coupling constants of electron and τ as described in Chapter 2.

At the present time, LEP, an electron-positron collider in Europe, has been running at the Z^0 pole energy region (around 91 GeV) and they determine the electroweak parameters very precisely. While the Z^0 exchange dominates in the τ pair process at the LEP energy region, the γ-Z interference effects are large at the TRISTAN energy region. Thus our results are complementary to those of LEP.

[1]The Standard Model is briefly described in Chapter 2

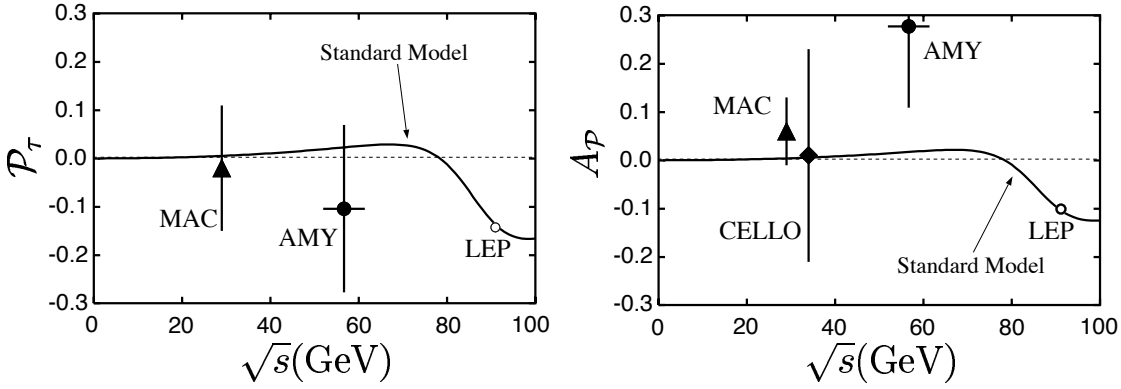

Figure 1.1: Results from other experiments on $\mathcal{P}_\tau$(left) and $A_\mathcal{P}$(right)[2, 3, 4, 5]. Solid line shows the Standard Model expectation. For the measurements at LEP, the values are averaged over four experiments and errors are close to the size of circles[5].

So far there are a few measurements of $\mathcal{P}_\tau$ and $A_\mathcal{P}$[2, 3, 4, 5], which are shown in Figure 1.1 together with the Standard Model expectation. As shown in the figure, $\mathcal{P}_\tau$ and $A_\mathcal{P}$ are expected to be very small in the Standard Model since the vector coupling of charged leptons to Z^0 is small: $\mathcal{P}_\tau = +2.8\%$ and $A_\mathcal{P} = +2.1\%$ are expected at the TRISTAN energy($\sqrt{s} = 58$ GeV). In addition, the values of $\mathcal{P}_\tau$ and $A_\mathcal{P}$ previously measured below Z^0 pole have relatively large errors because of small cross section there. VENUS has already stored the data of about 300 pb^{-1} corresponding to about 10000 τ pairs and it is possible and important to measure the average polarization and its forward-backward asymmetry of the τ lepton at the TRISTAN energy region.

This analysis employs data taken at center-of-mass energy of $\sqrt{s} = 58$GeV recorded by the VENUS detector from 1991 to 1995, representing a total integrated luminosity of 271 pb^{-1}. For the measurement of $\mathcal{P}_\tau$ and $A_\mathcal{P}$, four decay channels ($\tau \to \rho\nu, \pi(K)\nu, \mu\bar{\nu}\nu, e\bar{\nu}\nu$), which have relatively large branching fraction, have been investigated to obtain clean and large data sample. In the course of the analysis, the branching fractions of these decay channels of τ lepton are also measured.

Followings are the layout of this thesis. Chapter 2 contains a brief theoretical review of τ polarization for $e^+e^- \to \tau^+\tau^-$ process. The cross section for the process with unpolarized beam is briefly explained and the average polarization and its forward-backward asymmetry formulas are figured out.

In Chapter 3, methods to measure the polarization effect in the VENUS experiments are explained. Results from previous experiments are also summarized. TRISTAN accelerator and VENUS detector including trigger and data acquisition system are briefly summarized in Chapter 4. Selection of τ pair events and identification of decay modes are

described in Chapter 6. Measurement of the branching fractions is also described there. Evaluation of τ polarization and vector coupling constants of electron and τ are given in Chapter 7.

Finally Chapter 8 concludes the thesis.

Chapter 2

Theoretical review

2.1 The Standard Model of elementary particle physics

Since ancient times the human have been looking for the answer to the question what the world is made of. This motivation made us discover more than 100 atoms in the previous century, but people thought that it was too complicated to call them fundamental and that atoms had to have a deeper substructure. Indeed substructures of the material are consequently discovered: atoms are built up with electrons and nuclei, and nuclei are composed of protons and neutrons.

The elementary particle physics is a discipline to study constituents of material at the smallest dimension. Now we have a probable answer called "The Standard Model", which describes the world in terms of quarks, leptons (Table 2.1) and gauge bosons (Table 2.2). In this model, baryons and mesons, which are general terms to describe protons and pions and their kind, are composed of quarks. Both quarks and leptons are classified into three generations. Left-handed leptons and quarks form doublets of weak isospin, while right-handed ones are in isosinglet states.

Interactions between fermions are described by gauge theories in which interactions among particles are mediated by the gauge bosons listed in Table 2.2. The electromagnetic interaction is mediated by the photon(γ), the weak interactions by $W^{\pm}$, Z^0 and the strong and gravitational interactions by gluon and graviton, respectively. The oldest gauge theory is the quantum electrodynamics(QED). QED has two important properties, *i.e.* gauge invariance and renormalizability, and it predicts phenomena with electromagnetic interactions very precisely.

The electroweak model unifies the electromagnetic and weak interactions. This gauge theory, which is proposed by Glashow, Weinberg and Salam, is based on the symmetry group $\mathrm{SU}(2)_L \times \mathrm{U}(1)$ [7]. In the electroweak theory, it is thought that massless gauge

Quarks			Leptons		
$\begin{pmatrix} u \\ d \end{pmatrix}_L$	$\begin{pmatrix} c \\ s \end{pmatrix}_L$	$\begin{pmatrix} t \\ b \end{pmatrix}_L$	$\begin{pmatrix} \nu_e \\ e \end{pmatrix}_L$	$\begin{pmatrix} \nu_\mu \\ \mu \end{pmatrix}_L$	$\begin{pmatrix} \nu_\tau \\ \tau \end{pmatrix}_L$
u_R	c_R	t_R	$-$	$-$	$-$
d_R	s_R	b_R	e_R	μ_R	τ_R

Table 2.1: Fundamental fermions in the Standard Model.

Interaction	Gauge boson	Charge	Spin	Range (cm)
Electromagnetic	γ	0	1	∞
Weak	$W^{\pm}$, Z^0	± 1, 0	1	$\sim 10^{-16}$
Strong	gluon	0	1	$\sim 10^{-13}$
Gravitational	graviton	0	2	∞

Table 2.2: Gauge bosons.

bosons acquire their masses through a vacuum expectation value of a Higgs field [8]. The electroweak theory predicts the massive charged W and neutral Z bosons. Historically, the charged current process with $W^{\pm}$ exchange was first observed in nuclear β decay. The first example of weak neutral current process $\bar{\nu}_{\mu}e \rightarrow \bar{\nu}_{\mu}e$ was observed in heavy-liquid bubble chamber Gargamelle at CERN irradiated with a $\bar{\nu}_{\mu}$ beam[9]. The direct observation of the weak bosons was made for the first time at the CERN $p\overline{p}$ collider[10]. Since then, a lot of experimental studies using e^+e^- colliders such as PEP and PETRA have been carried out to check the electroweak theory.

2.2 e^+e^- annihilation process in The Standard Model

The lepton pair production process in e^+e^- annihilation is mediated by a virtual photon γ or a virtual neutral weak vector boson Z^0. In μ or τ pair production, only s-channel annihilation reaction can contribute to the process(Figure 2.1). Since the weak neutral current is a mixture of vector and axial-vector currents, the Lagrangian for this process in the Standard electroweak theory is written as

$$L_{f\overline{f}} = ieq_f\overline{u}_f\gamma^{\mu}u_fA_{\mu} + i\frac{g}{2\cos\theta_W}\overline{u}_f\gamma^{\mu}(g_V^f - g_A^f\gamma^5)u_fZ_{\mu}^{\mathrm{o}}. \tag{2.1}$$

Here, suffix f denotes the final state lepton, u_f represents a Dirac spinor of the lepton f, $A_{\mu}(Z_{\mu}^0)$ is the field of photon(neutral vector boson) and $e(g)$ is the electromagnetic(weak) coupling constants. q_f is the electric charge of the lepton in units of electron charge magnitude, where $q_f = -1$ for charged leptons. g_V^f and g_A^f are dimensionless vector and axial-vector coupling constants. The first and second term of Eq.(2.1) correspond to the electromagnetic interaction and the weak interaction, respectively.

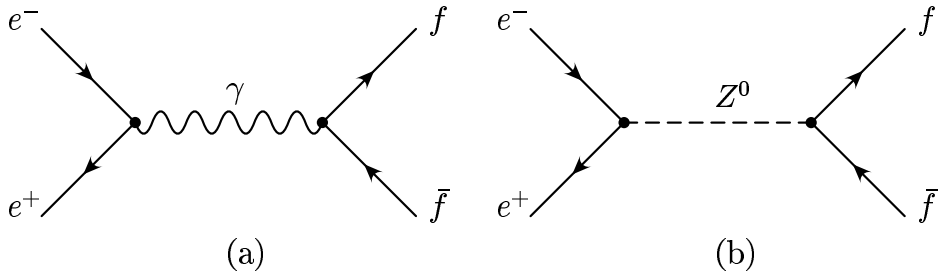

Figure 2.1: The lowest order Feynman diagrams contributing to s-channel lepton pair production mediated by (a):γ, (b):Z^0

The coupling constants e and g are related to each other by the weak angle θ_W,

$$e = g \sin\theta_W. \tag{2.2}$$

The Standard Model predicts the values of g_V^f and g_A^f as,

$$\begin{aligned} g_V^f &= I_3 - 2Q_f \sin^2\theta_W, \\ g_A^f &= I_3, \end{aligned} \tag{2.3}$$

where I_3 is the third component of the weak isospin of the fermion f and Q_f is its electric charge in units of electron charge magnitude. The explicit values of Q_f, g_V^f and g_A^f are listed in Table 2.3.

$\sin^2\theta_W$ is measured by several experiments to be about 0.23, which results in the very small value of vector coupling constant g_V^f for charged leptons.

Fermion	Q_f	g_V^f	g_A^f
ν_e, ν_μ, ν_τ	0	$\frac{1}{2}$	$\frac{1}{2}$
e^-, μ^-, τ^-	-1	$-\frac{1}{2} + 2\sin^2\theta_W \simeq -0.036$	$-\frac{1}{2}$
u, c, t	$\frac{2}{3}$	$\frac{1}{2} - \frac{4}{3}\sin^2\theta_W \simeq 0.191$	$\frac{1}{2}$
d, s, b	$-\frac{1}{3}$	$-\frac{1}{2} + \frac{2}{3}\sin^2\theta_W \simeq -0.345$	$-\frac{1}{2}$

Table 2.3: Charge and coupling constants of fermions(with $\sin^2\theta_W = 0.2319$).

2.3 Cross Section for $e^+e^- \to \tau^+\tau^-$process with unpolarized beam

The differential cross section for $e^+e^- \to \tau^+\tau^-$at high energies with unpolarized electron and positron beam can be calculated by Eq.(2.1) with the approximation of $\sqrt{s} \gg m_\tau$, where $\sqrt{s}$ means the center-of-mass energy of colliding e^+e^- system: $\sqrt{s} = 2E_{\text{beam}}$.

$$\frac{d\sigma}{d\Omega}(\cos\theta, h) = \frac{\alpha^2}{8s}[F_0(s)(1+\cos^2\theta) + 2F_1(s)\cos\theta - h\{F_2(s)(1+\cos^2\theta) + 2F_3(s)\cos\theta\}], \tag{2.4}$$

where $h(=\pm 1)$ is the helicity of τ^- and θ is the scattering angle between e^- and τ^-. The factors F_0, F_1, F_2, F_3 are given as

$$\begin{aligned}
F_0(s) &= 1 + 2g_V^e g_V^\tau \mathrm{Re}\chi(s) + (g_V^{e2} + g_A^{e2})(g_V^{\tau 2} + g_A^{\tau 2})|\chi(s)|^2, \\
F_1(s) &= 2g_A^e g_A^\tau \mathrm{Re}\chi(s) + 4g_V^e g_A^e g_V^\tau g_A^\tau |\chi(s)|^2, \\
F_2(s) &= 2g_V^e g_A^\tau \mathrm{Re}\chi(s) + 2(g_V^{e2} + g_A^{e2}) g_V^\tau g_A^\tau |\chi(s)|^2, \\
F_3(s) &= 2g_A^e g_V^\tau \mathrm{Re}\chi(s) + 2g_V^e g_A^e (g_V^{\tau 2} + g_A^{\tau 2})|\chi(s)|^2,
\end{aligned} \tag{2.5}$$

where $\mathrm{Re}\chi(s)$ terms are the contributions of the interferences between two diagrams in Figure 2.1 and $|\chi(s)|^2$ terms are the contributions of Figure 2.1(b). It is noticeable that the interference has the biggest contribution at the TRISTAN energy region in the lepton(μ or τ) pair production process: the magnitude of $\mathrm{Re}\chi(s)$ at TRISTAN is four or six times larger than that at PEP[1] or PETRA[2], respectively.
In the Standard Model, the function $\chi(s)$ can be written as

$$\chi(s) = \frac{1}{4\sin^2\theta_W \cos^2\theta_W} \times \frac{s}{s - M_Z^2 + is\Gamma_Z/M_Z}, \tag{2.6}$$

where M_Z and Γ_Z is the mass and width of the neutral vector boson Z^0, respectively.

The longitudinal τ polarization is then defined and calculated as follows:

$$\mathcal{P}_\tau(s, \cos\theta) = \frac{\frac{d\sigma}{d\Omega}(h=+1) - \frac{d\sigma}{d\Omega}(h=-1)}{\frac{d\sigma}{d\Omega}(h=+1) + \frac{d\sigma}{d\Omega}(h=-1)} \tag{2.7}$$

$$= -\frac{(1+\cos^2\theta)F_2(s) + 2\cos\theta F_3(s)}{(1+\cos^2\theta)F_0(s) + 2\cos\theta F_1(s)} \tag{2.8}$$

2.4 Average polarization and its forward-backward asymmetry

Average τ polarization $\mathcal{P}_\tau$ can be obtained by integrating each differential cross section term in Eq. (2.7) as,

$$\mathcal{P}_\tau = \frac{(\sigma_R)_i - (\sigma_L)_i}{(\sigma_R)_i + (\sigma_L)_i}, \tag{2.9}$$

where

$$(\sigma_{R(L)})_i = \int_i \frac{d\sigma(h, s, \cos\theta)}{d\cos\theta} \tag{2.10}$$

[1] An e^+e^- collider in US which was operated during 1980-1990 at $\sqrt{s} = 30$ GeV.
[2] An e^+e^- collider in Germany which was operated during 1978-1986 at $\sqrt{s} = 14 \sim 46$ GeV

are the cross sections for production of right-(left-) handed τ^- with appropriate integration for $i = T, F, B(T$:Total, F:Forward, B:Backward).

The forward-backward asymmetry of the polarization is defined as,

$$A_{\mathcal{P}} = \frac{\sigma_F {\mathcal{P}_\tau}^F(s) - \sigma_B {\mathcal{P}_\tau}^B(s)}{\sigma_F + \sigma_B}. \tag{2.11}$$

where ${\mathcal{P}_\tau}^F(s)$ and ${\mathcal{P}_\tau}^B(s)$ denote the average τ polarizations in the forward and backward region, respectively.

Using Eqs. (2.4-2.10), the average polarization and its forward-backward asymmetry can be expressed in terms of $F_i(i$=0,1,2,3) as

$$\begin{aligned} \mathcal{P}_\tau(s) &= -\frac{F_2(s)}{F_0(s)} \\ A_{\mathcal{P}}(s) &= -\frac{3}{4}\frac{F_3(s)}{F_0(s)}. \end{aligned} \tag{2.12}$$

These can be approximated by assuming $s \ll M_Z^2$ in the energy region below Z^0 pole as

$$\begin{aligned} \mathcal{P}_\tau(s) &\approx -g_V^e g_A^\tau \mathrm{Re}\chi(s), \\ A_{\mathcal{P}}(s) &\approx -\frac{3}{4} g_V^\tau g_A^e \mathrm{Re}\chi(s). \end{aligned} \tag{2.13}$$

Here, the axial vector coupling constants g_A^τ and g_A^e can be evaluated by measuring the total and differential cross sections of $e^+e^- \to \tau^+\tau^-$, which makes $\mathcal{P}_\tau$ and $A_{\mathcal{P}}$ sensitive to the vector coupling constants g_V^τ and g_V^e. Solid lines in Figure 1.1 show the Standard Model expectations of the average τ polarization and its forward-backward asymmetry as function of $\sqrt{s}$.

2.5 Importance of the measurement of $\mathcal{P}_\tau$ and $A_{\mathcal{P}}$ at TRISTAN

The measurement of $\mathcal{P}_\tau$ and $A_{\mathcal{P}}$ makes it possible to confirm the framework of the Standard Model in the least model independent manner. The real part of $\chi(s)(\mathrm{Re}\chi(s))$ dominates the τ polarization and its forward-backward asymmetry in the energy region below Z^0 as Eq.(2.13) using Eqs.(2.5), (2.6) and (2.12). On the other hand, $\mathrm{Re}\chi(s)$ terms vanishes and only $|\chi(s)|^2$ terms contribute to $\mathcal{P}_\tau$ and $A_{\mathcal{P}}$ in the energy region around Z^0 pole($s \approx M_Z^2$) as

$$\begin{aligned} \mathcal{P}_\tau(s) &\approx -\frac{2(g_V^{e2} + g_A^{e2}) g_V^\tau g_A^\tau |\chi(s)|^2}{(g_V^{e2} + g_A^{e2})(g_V^{\tau 2} + g_A^{\tau 2})|\chi(s)|^2} = -\frac{2 g_V^\tau g_A^\tau}{g_V^{\tau 2} + g_A^{\tau 2}}, \\ A_{\mathcal{P}}(s) &\approx -\frac{3}{4}\frac{2 g_V^e g_A^e (g_V^{\tau 2} + g_A^{\tau 2})|\chi(s)|^2}{(g_V^{e2} + g_A^{e2})(g_V^{\tau 2} + g_A^{\tau 2})|\chi(s)|^2} = -\frac{3}{4}\frac{2 g_V^e g_A^e}{g_V^{e2} + g_A^{e2}}. \end{aligned}$$

In other words, the interference between the γ-mediated process(Figure 2.1(a)) and the Z^0-mediated process(Figure 2.1(b)) is important in the energy region below Z^0 pole, while only the Z^0-mediated process contributes in the energy region around Z^0 pole.

Thus, it is very important for the test of the Standard Model to measure the τ polarization and its forward-backward asymmetry at the TRISTAN energy region, where the interference term has the biggest contribution.

Chapter 3

Experimental point of view

3.1 Observables sensitive to the τ polarization

Due to the $V-A$ structure of the weak charged current decay of τ lepton, the τ polarization can be deduced from an analysis of the kinematical distribution of decay products, such as the angular distribution in the τ rest frame[12]. In the analysis presented here, four major 1-prong decay modes are studied: $\tau \to e\bar{\nu}_e\nu_\tau$, $\tau \to \mu\bar{\nu}_\mu\nu_\tau$, $\tau \to \pi(K)\nu_\tau$, $\tau \to \rho\nu_\tau$ which amount about 70 % of all τ decays[13]. It is not possible to separate π from K with the VENUS detector and they are treated as "π" in the present analysis[1]. Here, '1-prong' means that a τ lepton decays to one charged particle and one or more neutral particles, which we observe one track in tracking detector because only charged particles can leave their trajectories in the detector. Similarly, a τ decay to n charged particles and one or more neutral particles is called 'n-prong'.

3.1.1 Leptonic decay modes

In the leptonic decay modes, the decay angles cannot be reconstructed since there are two missing ν's. Only the momentum distributions of the electron or the μ are measured in the laboratory frame. In the approximation of $m_{e,\mu}/m_\tau \ll 1$ and $m_\tau/m_Z \ll 1$, they are given in terms of $\mathcal{P}_\tau$ by[11],

$$W = \frac{1}{3}[(5 - 9x^2 + 4x^3) + \mathcal{P}_\tau(1 - 9x^2 + 8x^3)]. \tag{3.1}$$

The fractional momentum $x = p_{\text{charged}}/E_{\text{beam}}$ is used throughout this thesis to denote momenta of particles in the laboratory system.

[1]The branching fraction of $\tau \to K\nu$ mode is very small(1.7 %) because of Cabibbo supression. This is the reason why we can treat both π and K together.

3.1.2 Hadronic decay modes

For the hadronic decay modes, the distribution of the decay angle ψ_τ of the hadron in the τ rest frame relative to the τ flight direction is given by[12],

$$W = 1 + \alpha \mathcal{P}_\tau \cos\psi_\tau, \tag{3.2}$$

with $\alpha = 1$ for spin-0 particles($\pi(K)$) and $\alpha = (m_\tau^2 - 2m^2)/(m_\tau^2 + m^2)(= 0.46)$ for spin-1 particles(ρ), where m_τ and m are the masses of the τ and the hadronic system, respectively. The angle ψ_τ can be expressed in terms of the fractional hadron momentum x in the laboratory system:

$$\cos\psi_\tau = \frac{2x - 1 - m^2/m_\tau^2}{1 - m^2/m_\tau^2}. \tag{3.3}$$

Eq. (3.2) can be recast by neglecting the mass of the daughter hadron compared to the mass of τ in Eq. (3.3) as:

$$W = 1 + \alpha \mathcal{P}_\tau (2x - 1), \tag{3.4}$$

which enables us to deduce the τ polarization by measuring the momentum distribution of the $\pi(K)$ or ρ.

Here, the reduction of the analyzing power for ρ by the factor $\alpha = 0.46$ is due to the contribution of both longitudinal and transverse spin states of the ρ meson. However, this reduction can be compensated by separating the spin states of ρ meson with the introduction of the second angle ψ_ρ which characterizes the decay distribution of ρ meson itself into $\pi^\pm\pi^0$ [14, 15]. The angle ψ_ρ is the decay angle of the 2π system in the ρ rest frame relative to the ρ flight direction, which is given in terms of the energies of the two pions in the laboratory system as

$$\cos\psi_\rho = \frac{m_\rho}{\sqrt{m_\rho^2 - 4m_\pi^2}} \frac{E_\pi - E_{\pi^0}}{|\vec{p_\pi} + \vec{p_{\pi^0}}|}. \tag{3.5}$$

3.1.3 Expected distribution for $\mathcal{P}_\tau = \pm 1$

Summarizing above discussions, observables which are sensitive to the τ polarization are the fractional momentum x distribution for $\tau \to e\bar{\nu}\nu$, $\tau \to \mu\bar{\nu}\nu$, $\tau \to \pi(K)\nu$ and the two-dimensional distribution of ψ_τ and ψ_ρ in this analysis.

Fig. 3.1 and 3.2 show such distributions for fully polarized($\mathcal{P}_\tau = \pm 1$) and unpolarized($\mathcal{P}_\tau = 0$) τ lepton decay.

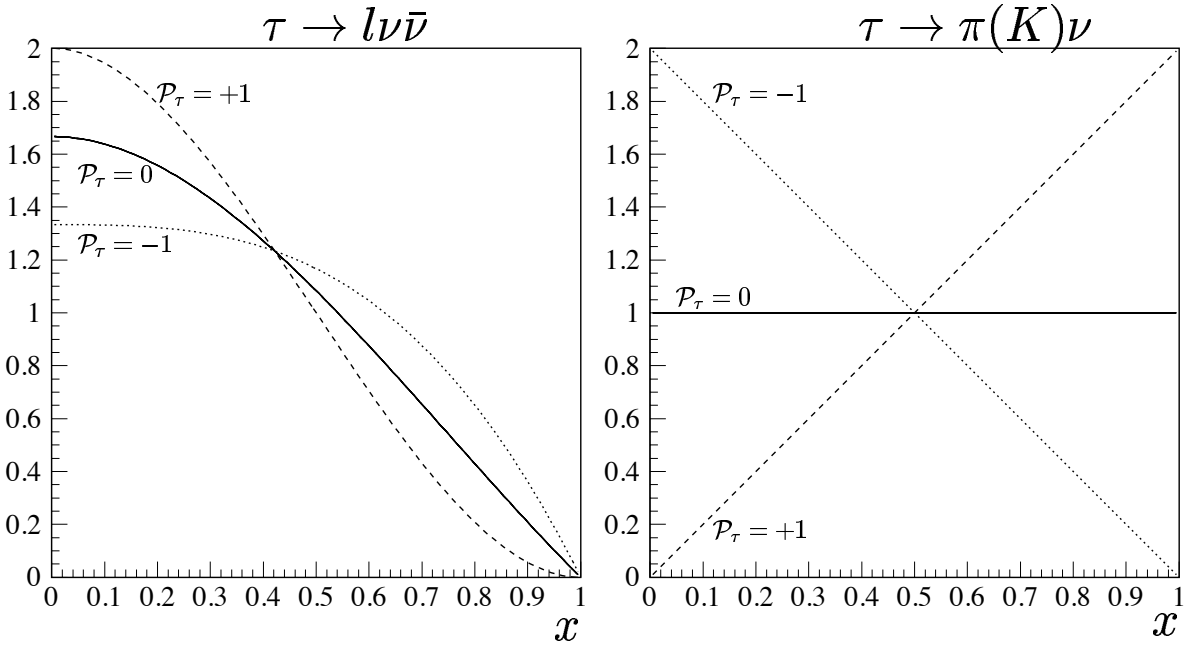

Figure 3.1: x distributions for leptonic decay modes(left) and $\tau \to \pi(K)\nu$ mode(right). Dotted line is the distribution for -100 % τ polarization, dashed line for $+100$ % τ polarization and solid line for unpolarized τ.

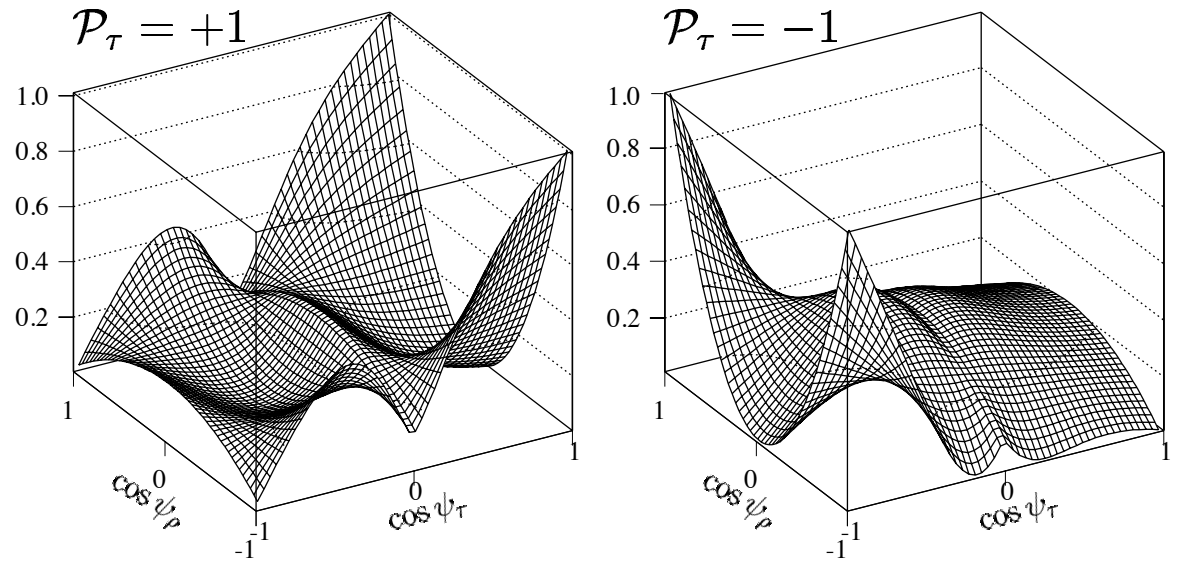

Figure 3.2: two-dimensional distributions in ψ_τ and ψ_ρ for $\tau \to \rho\nu$ mode for $+100$ % τ polarization(left) and -100 % τ polarization(right).

3.2 Practical method to measure the τ polarization

In principle, the τ polarization can be deduced by fitting the measured distribution with the theoretical formula such as Eq. (3.1) or (3.4). However such method is not practical because of following two reasons:

- Measured distribution is distorted by the detector acceptance and the detection efficiencies for the specific τ-decay mode.
- Initial state radiation distort the theoretical formula such as Eq. (3.1) or (3.4) because it change the center-of-mass energy and therefore change the τ momentum. Fig. 3.3 shows such effect for $\tau \to \pi\nu$ mode: If τ is not polarized, theoretical x distribution is flat(dashed line in Fig. 3.3), which is distorted by the radiative corrections as solid line histogram in Fig. 3.3.

Although the acceptance and efficiency effects can be corrected by the study with the Monte Carlo events, it is difficult to correct the radiative effects. To be practical *i.e.* to take into account the acceptance, efficiency and radiative effects simultaneously, the τ polarization is measured by obtaining the linear combination of two fully polarized($\mathcal{P}_\tau = \pm 1$) Monte Carlo distributions which account for all the practical distortion of Eq.(3.1) or (3.4).

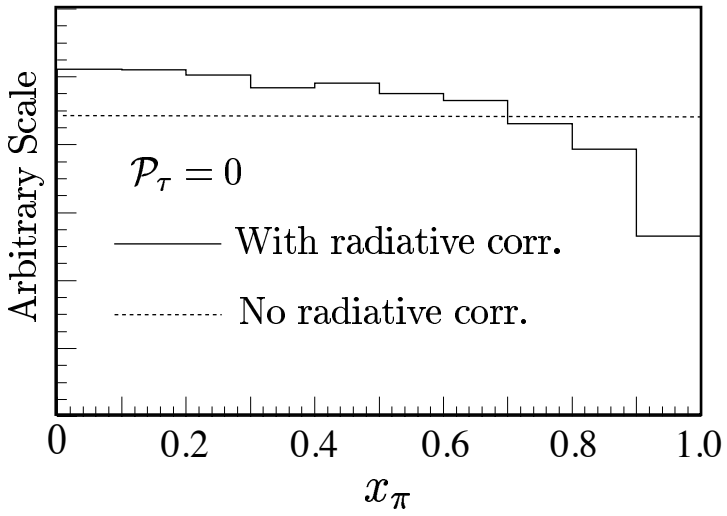

Figure 3.3: x distribution for $\tau \to \pi\nu$ mode created by using the Monte Carlo events. Solid line histogram shows the distortion of a theoretical expectation(dotted line) by radiative corrections.

3.3 Results from Other Experiments

There have been three results below Z^0 pole[2, 3, 4] and four results on Z^0 pole from LEP(ALEPH[16], DELPHI[17], OPAL[18] and L3[19]) on the τ polarization as summarized in Table 3.1.

The three *old* experiments used the x distributions for $\tau \to e\bar{\nu}\nu, \mu\bar{\nu}\nu, \pi(K)\nu, \rho\nu$ modes to evaluate $\mathcal{P}_\tau$ and $A_\mathcal{P}$ by fitting the x distribution with theoretical formula Eq.((3.1) or (3.4)) after correcting the effects of acceptances, efficiencies and radiative corrections. Corrections of radiative effects in their experiments were made bin-by-bin in x distributions for each decay mode by comparing the Monte Carlo data with and without radiative effects, which is very sensitive to the imperfect modelling of the radiative corrections. On the other hand, the method used in the present analysis, which is described in the previous section, is less sensitive to the implementation of the radiative corrections.

In four LEP experiments, five τ decay modes($\tau \to e\bar{\nu}\nu, \mu\bar{\nu}\nu, \pi(K)\nu, \rho\nu$ and $a_1\nu$) were studied and results on $\mathcal{P}_\tau$ and $A_\mathcal{P}$ were evaluated by using the same method as applied in the present analysis[5, 16, 17, 19, 18]. The results which were averaged over four experiments are also tabulated.

As found in the Table, there is no substantial measurement on $\mathcal{P}_\tau$ and $A_\mathcal{P}$ below Z^0 pole and it is, therefore, very important to make their precise measurement at the TRISTAN energy.

	$\mathcal{P}_\tau$	$A_\mathcal{P}$	$\sqrt{s}$(GeV)	Accelerator
MAC[2]	$-0.02 \pm 0.07 \pm 0.11$	$(0.06 \pm 0.07) \times (1 \pm 0.011)$	29	PEP
CELLO[3]	-	0.01 ± 0.22	34	PETRA
AMY[4]	-0.104 ± 0.173	0.277 ± 0.168	52-61.4	TRISTAN
ALEPH[16]	$-0.137 \pm 0.012 \pm 0.008$	$-0.095 \pm 0.012 \pm 0.004$		
DELPHI[17]	$-0.144 \pm 0.018 \pm 0.016$	$-0.105 \pm 0.021 \pm 0.002$		
OPAL[18]	$-0.153 \pm 0.019 \pm 0.013$	$-0.092 \pm 0.023 \pm 0.009$	$\sim$91	LEP
L3[19]	$-0.150 \pm 0.013 \pm 0.009$	$-0.118 \pm 0.015 \pm 0.004$		
LEP global[5]	-0.145 ± 0.009	-0.103 ± 0.008		

Table 3.1: Results from other experiments on $\mathcal{P}_\tau$ and $A_\mathcal{P}$.

3.4 Acceptance and $A_{\mathcal{P}}$

It must be noted that the experimental acceptance should be considered for the calculation of the polarization asymmetry $A_{\mathcal{P}}$. The forward region is defined as $\theta_{\rm min} \leq \theta \leq \frac{\pi}{2}$ and the backward region as $\frac{\pi}{2} < \theta \leq \pi - \theta_{\rm min}$, where $\theta_{\rm min}$ is the minimum detection angle.

The τ polarization in the forward and backward region, ${\mathcal{P}_\tau}^F(s)$ and ${\mathcal{P}_\tau}^B(s)$, is expressed by using $\theta_{\rm min}$ as

$$ {\mathcal{P}_\tau}^F(s) = -\frac{F_2(s)(\cos\theta_{\rm min} + \frac{1}{3}\cos^3\theta_{\rm min}) + F_3(s)\cos^2\theta_{\rm min}}{F_0(s)(\cos\theta_{\rm min} + \frac{1}{3}\cos^3\theta_{\rm min}) + F_1(s)\cos^2\theta_{\rm min}} \tag{3.6} $$

$$ {\mathcal{P}_\tau}^B(s) = -\frac{F_2(s)(\cos\theta_{\rm min} + \frac{1}{3}\cos^3\theta_{\rm min}) - F_3(s)\cos^2\theta_{\rm min}}{F_0(s)(\cos\theta_{\rm min} + \frac{1}{3}\cos^3\theta_{\rm min}) - F_1(s)\cos^2\theta_{\rm min}}. \tag{3.7} $$

As described in Chapter 4, the minimum detection angle in the present analysis is limited by the muon chamber to be $\cos\theta_{\rm min} = 0.5$.

Chapter 4

Experimental Apparatus

Data used in the present analysis were collected with the VENUS detector at the electron-positron collider TRISTAN. A brief introduction of the TRISTAN accelerator and the VENUS detector is given below.

4.1 TRISTAN

4.1.1 Overview

After commissioning of TRISTAN in 1986, a great deal of effort has been put in raising the energy of TRISTAN as high as possible (TRISTAN Phase-I). To achieve this goal, more than thirty cavities were installed at TRISTAN until the summer of 1989. Thus, the maximum beam energy of 32 GeV was achieved.

In February 1991, TRISTAN Phase-II operation was started. In this Phase-II operation, the emphasis of the operation was placed on achieving as high integrated luminosity as possible. To increase the luminosity a pair of superconducting quadrupole magnets (QCSs) were installed at each collision point. The beam energy of TRISTAN was set at 29GeV in order to have a sufficient operational margin for radio frequency(RF) accelerator cavities and to minimize breakdown time of cavities which leads to the losses of the beam. TRISTAN Phase-II operation ended at 9:00 AM on May 10 1995. The total integrated luminosity collected with the VENUS detector reached about 400 pb^{-1}. This analysis employs data collected during the period of TRISTAN Phase-II because the τ polarization depends on the center-of-mass energy and also because of availability of a transition radiation detector(TRD) which is a powerful detector for the separation of electrons and pions as described later.

4.1.2 TRISTAN Accelerator

TRISTAN is a large electron-positron colliding beam facility at the National Laboratory for High Energy Physics (KEK) [20]. TRISTAN is operated at the center-of-mass energies around 58GeV at which large effects due to γ-Z interference appear. Fig. 4.1 illustrates a schematic view of TRISTAN.

Figure 4.1: The schematic view of TRISTAN.

4.1.2 TRISTAN Accelerator

TRISTAN is a large electron-positron colliding beam facility at the National Laboratory for High Energy Physics (KEK) [20]. TRISTAN is operated at the center-of-mass energies around 58GeV at which large effects due to γ-Z interference appear. Fig. 4.1 illustrates a schematic view of TRISTAN.

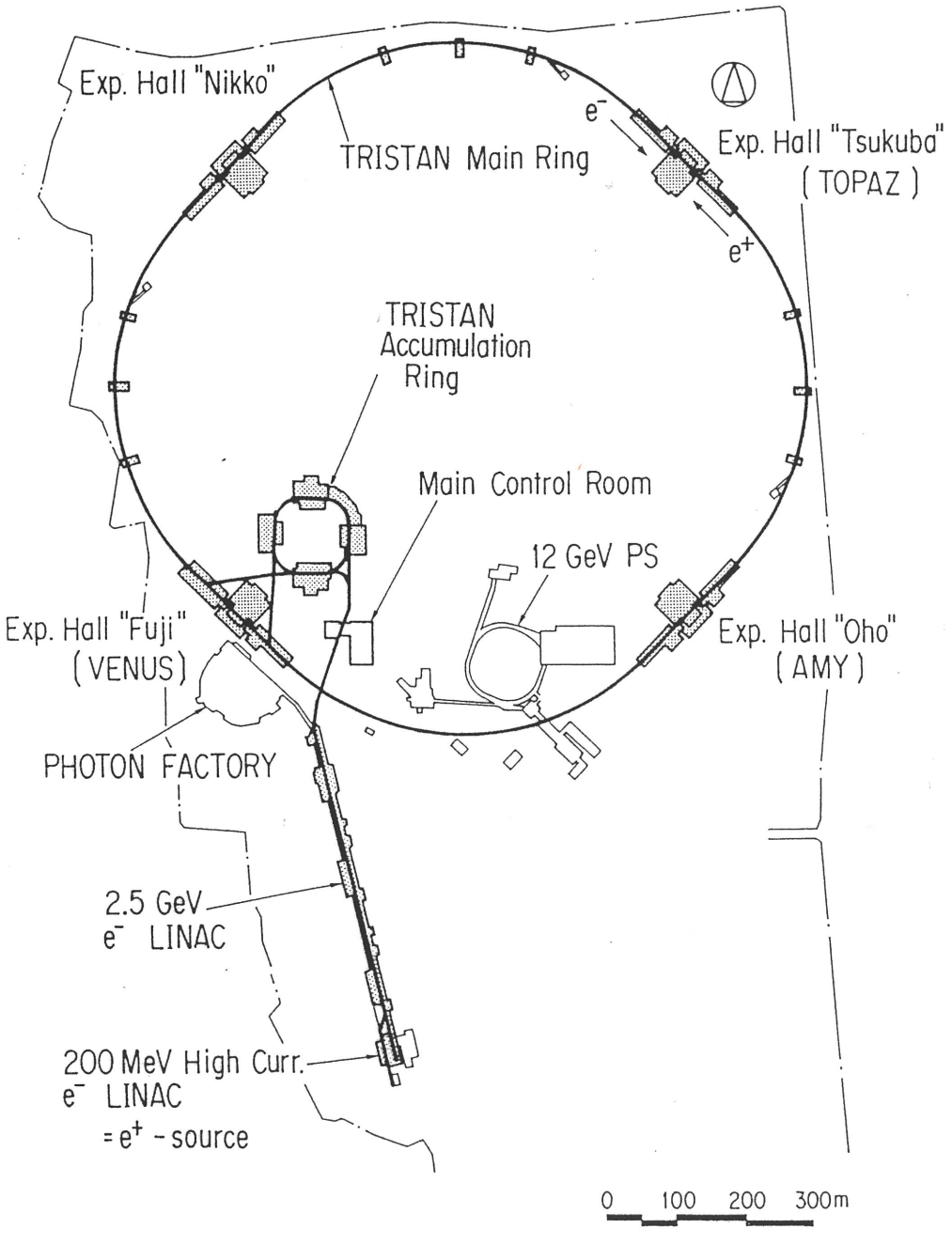

Figure 4.1: The schematic view of TRISTAN.

TRISTAN consists of three main components: a linear accelerator (LINAC), an accumulation ring (AR), and a main ring (MR). The LINAC is 400 m long and accelerates electrons and positrons up to 2.5 GeV. Positrons are produced by bombarding a tantalum target with a high-current electron beam of 200 MeV from a linear accelerator placed at the upstream end of the LINAC, and are then accelerated to 250 MeV by another linear accelerator located downstream of the conversion target prior to transferring to the LINAC. Electrons and positrons accelerated in the LINAC are injected and accumulated in the AR. The AR is a booster whose circumference is 377 m and stores electrons or positrons from the LINAC to the beam current higher than 10 mA. After the accumulation, the electron or positron beam is accelerated up to 8.0 GeV and then injected into the MR. The MR has a 3018 m circumference and has four straight sections of 193 m length. Two electron and two positron bunches circulate in opposite directions and collide with each other at the mid-points of the straight sections where the colliding beam detectors are located. The bunches collide every 5 μs. A large portion of the straight section is allocated for radio frequency accelerator cavities ($f_{RF} = 508.6$ MHz) which accelerate the beams from the injection energy to the required collision energy and compensate for large loss of energy due to synchrotron radiation. The loss of energy(ΔE) due to synchrotron radiation is expressed by the formula

$$\Delta E \cong 0.0885 \times \frac{{E_b}^4}{\rho}(\mathrm{MeV}/turn), \tag{4.1}$$

where E_b denotes the beam energy in GeV and ρ is the radius of curvature in m. The energy spread σ_E of the beam is expressed as

$$\frac{\sigma_E}{E} = 0.857 \times 10^{-3} \times \frac{E_b}{\rho}, \tag{4.2}$$

which amounts to 49 MeV at $E_b = 29$ GeV. The energy spread varies according to the frequency shift (Δf) applied to the accelerator by radio frequency accelerator cavities. Δf is fixed at 3 kHz during the runs analyzed in the present study.

The beam bunch has approximately a Gaussian shapes with effective r.m.s. width of about 0.3 mm in the horizontal direction, 10 μm in the vertical direction, and 20 mm in the beam direction at the intersection points in the TRISTAN Phase-II operation. The parameters of the TRISTAN-MR are listed in Table 4.1. Among them, the luminosity is the most important parameter in the colliding beam experiments. The event rate, dN/dt, for a reaction having a total cross section σ, is related to the luminosity L of the machine by

TRISTAN-MR parameters	
Circumference	3018 m
Bending radius	246.5 m
Length of straight section	4×194.4 m
Injection beam energy	8.0 GeV
Maximum beam energy	32.0 GeV
RF frequency	508.6 MHz
Number of collision points	4
Number of bunches	$4(2e^{+}+2e^{-})$
Two e^{+} and e^{-} bunch current	13 mA
Beam size at collision point ($\sigma_x^*/\sigma_y^*/\sigma_z^*$)	2/0.05/20 mm
Maximum luminosity	5.0×10^{31} cm^{-2}s^{-1}
Maximum integrated luminosity per day	1.02 pb^{-1}
Beam life	4∼5 hours

Table 4.1: Parameters of TRISTAN-MR.

$$\frac{dN}{dt} = \mathrm{L} \cdot \sigma. \tag{4.3}$$

For an $e^{+}e^{-}$ collider, L is often expressed as follows:

$$L = \frac{I_{e^+} I_{e^-}}{4\pi e^2 N_b f \sigma_x{}^* \sigma_y{}^*}, \tag{4.4}$$

where

I_{e^+,e^-} : beam current,

N_b : number of bunches,

f : repetition rate (99.33 kHz for TRISTAN) ,

$\sigma_x{}^*$: horizontal r.m.s. beam size at the interaction point,

$\sigma_y{}^*$: vertical r.m.s. beam size at the interaction point.

In practice, the luminosity is determined by counting the number of Bhabha scattering(elastic scattering of electron and positron; $e^{+}e^{-} \to e^{+}e^{-}$) events.

4.2 The VENUS Detector

4.2.1 Overview

The VENUS detector is a general purpose magnetic spectrometer designed to study the various reactions in the e^+e^- annihilation [21]. From November 1986 to July 1990 (TRISTAN Phase-I), the maximum center-of-mass energy achieved was 64 GeV and the integrated luminosity accumulated during this period is 60 pb^{-1}. With the VENUS detector, tests of the Electroweak theory and searches for evidence of new physics beyond the Standard Model were performed. Thus, the energy frontier operation was completed. In February 1991, TRISTAN Phase-II operation was started. At the same time, new detector components were installed, namely a transition radiation detector (TRD) [22], a vertex chamber [23] and a trigger chamber as well as a new beam pipe and mask system in the VENUS detector. These new detectors contribute significantly to the improvement of analyses of physics which require high luminosity such as heavy quark or τ physics etc. The VENUS accumulated an integrated luminosity of about 300 pb^{-1} from February 1991 to May 1995. The present analysis is based on the data taken at the center-of-mass energy at 58 GeV during this period.

The characteristics of the VENUS detector are high resolution in tracking of charged particles, good electromagnetic calorimetry and high hermeticity. Especially, the electromagnetic calorimeters cover more than 99 % of 4π solid angle without any holes. Figure 4.2 and Figure 4.3 show a bird's eye view and a cross-sectional view of one quadrant of the VENUS detector, respectively.

Figure 4.2: Bird's eye view of the VENUS detector.

4.2 The VENUS Detector

4.2.1 Overview

The VENUS detector is a general purpose magnetic spectrometer designed to study the various reactions in the e^+e^- annihilation [21]. From November 1986 to July 1990 (TRISTAN Phase-I), the maximum center-of-mass energy achieved was 64 GeV and the integrated luminosity accumulated during this period is 60 pb^{-1}. With the VENUS detector, tests of the Electroweak theory and searches for evidence of new physics beyond the Standard Model were performed. Thus, the energy frontier operation was completed. In February 1991, TRISTAN Phase-II operation was started. At the same time, new detector components were installed, namely a transition radiation detector (TRD) [22], a vertex chamber [23] and a trigger chamber as well as a new beam pipe and mask system in the VENUS detector. These new detectors contribute significantly to the improvement of analyses of physics which require high luminosity such as heavy quark or τ physics etc. The VENUS accumulated an integrated luminosity of about 300 pb^{-1} from February 1991 to May 1995. The present analysis is based on the data taken at the center-of-mass energy at 58 GeV during this period.

The characteristics of the VENUS detector are high resolution in tracking of charged particles, good electromagnetic calorimetry and high hermeticity. Especially, the electromagnetic calorimeters cover more than 99 % of 4π solid angle without any holes. Figure 4.2 and Figure 4.3 show a bird's eye view and a cross-sectional view of one quadrant of the VENUS detector, respectively.

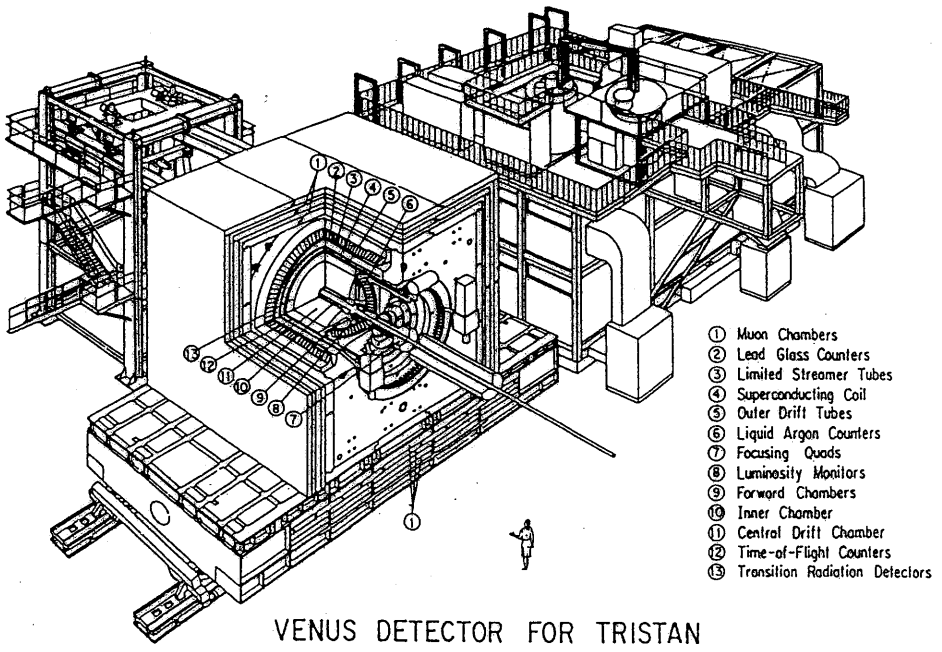

Figure 4.2: Bird's eye view of the VENUS detector.

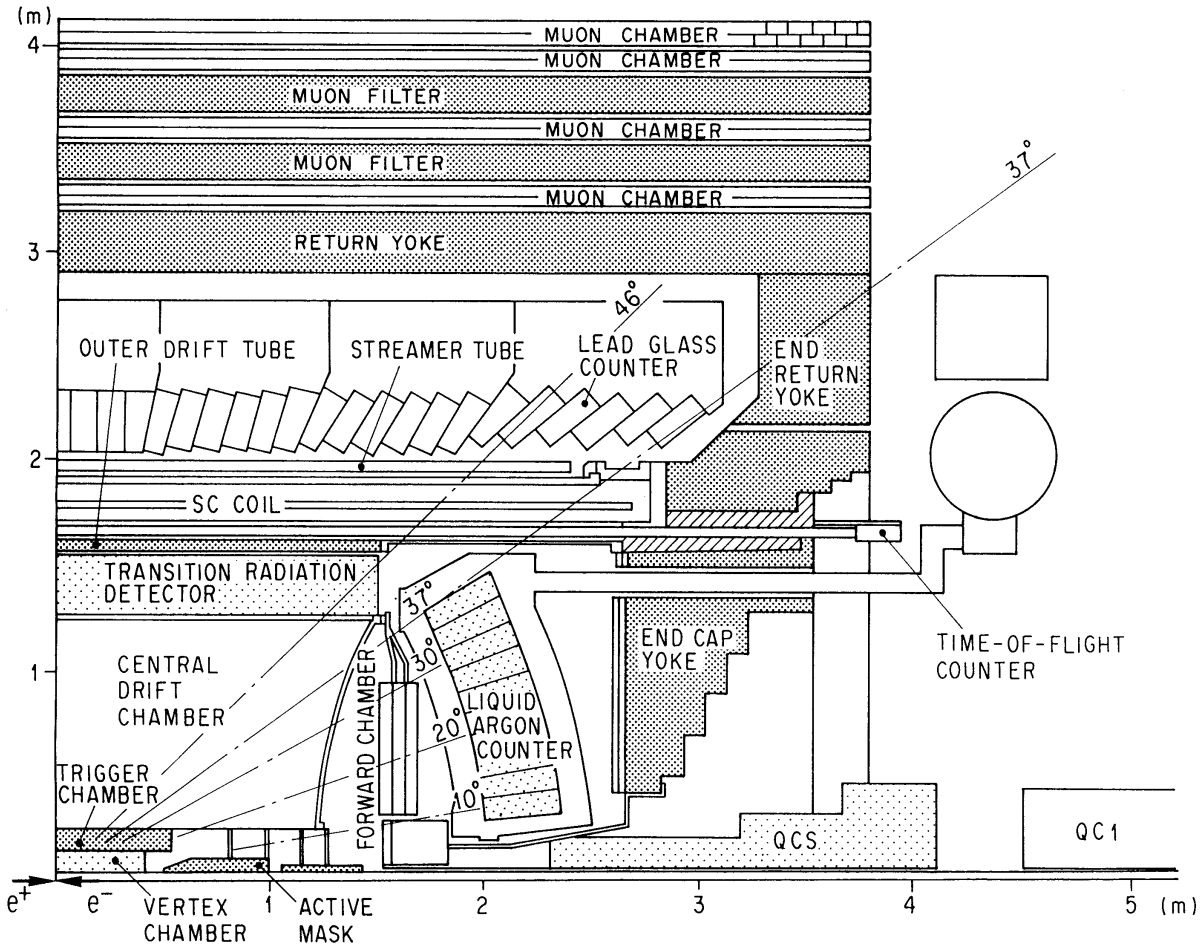

Figure 4.3: Cut through the VENUS detector along the beamline. Only one quadrant is shown.

The coordinate system for the detector geometry is taken to be the right-handed Cartesian as shown in Figure 4.4(a). The x-axis is horizontal and outward from the center of the TRISTAN ring, the y-axis is vertical and upward, and the z-axis is parallel to the direction of the electron beam. The origin of this system is the interaction point. Since most of the detector components are cylindrically symmetric with respect to the z-axis, we also define the cylindrical coordinate as shown in Figure 4.4(b). The polar angle θ is defined as the angle measured from the z-axis and the azimuthal angle ϕ is measured counterclockwise from the x-axis in the x-y plane.

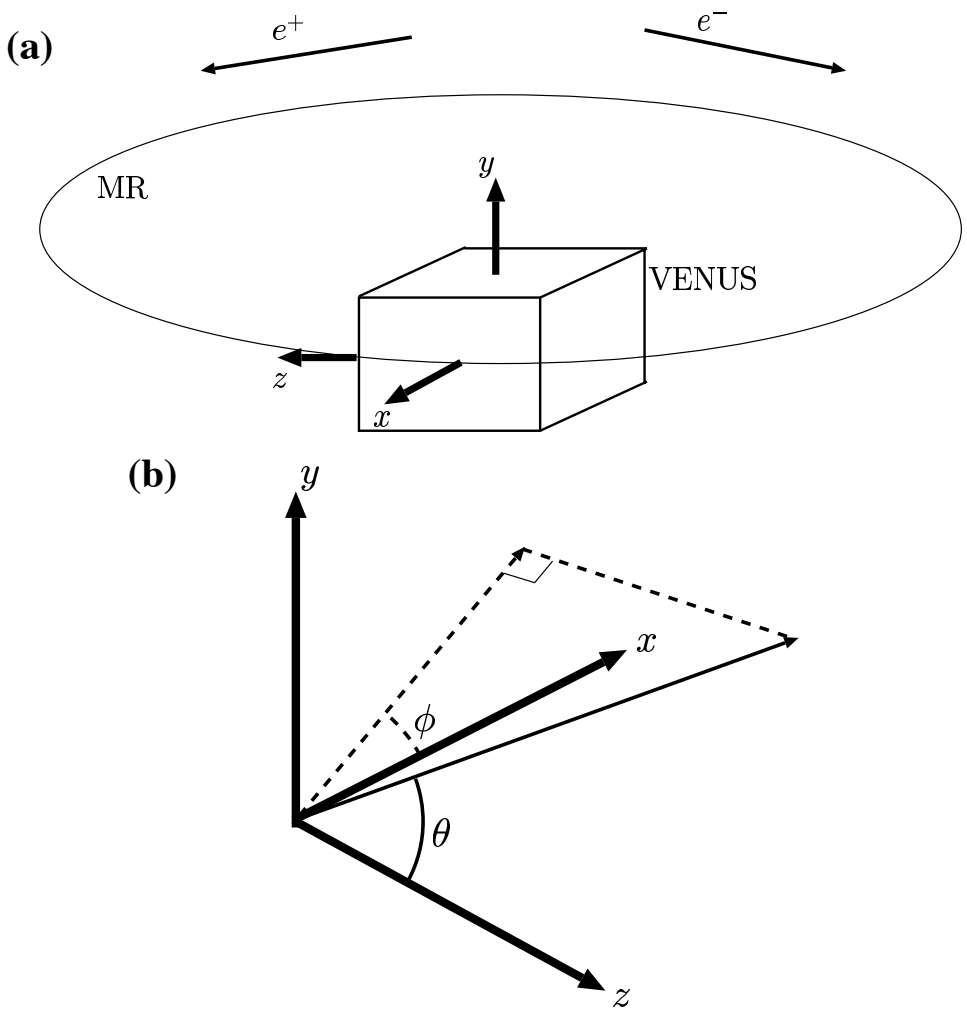

Figure 4.4: The definition of coordinates of the VENUS detector: (a) Cartesian coordinate and (b) cylindrical coordinate.

The VENUS detector consists of many subsystems to obtain complementary sets of information on the electron-positron interactions. In the present analysis, we use mainly the central drift chamber(CDC), the lead-glass calorimeter(LG), the end-cap liquid argon calorimeter(LA), the time-of-flight(TOF) counter system, the transition radiation detector(TRD) and the muon chamber(MU). Followings are brief descriptions of these components.

4.2.2 Central Drift Chamber

The central drift chamber(CDC)[24], which is a cylindrical multi-wire drift chamber, is the main tracking device of the VENUS detector. A schematic view of the CDC in the r-ϕ plane is shown in Figure 4.5.

Figure 4.5: The central drift chamber: quadrant part of an end view(left) and wire arrangement(right).

The dimension of the CDC is 300 cm in length with the inner radius of 25 cm and the outer radius of 126 cm. It consists of 7104 single-hit drift cells whose cross sections are about 2×2 cm^2. A unit cell has one anode wire, a gold plated tungsten wire with the diameter of 30 μm, and six cathode wires, gold-plated molybdenum wires with the diameter of 140 μm, as shown in Figure 4.5. There are twenty layers of axial wires parallel to the beam axis to measure the r-ϕ coordinates and nine layers of stereo wires which are slanted with an angle of $\pm3.5^\circ$ with respect to the beam axis to measure the z-coordinate of a track. As shown in Figure 4.5, two adjacent layers of axial wires are staggered by a half cell width. These 29 layers cover the polar angle range of $|\cos\theta| \leq 0.75$. The chamber is filled with HRS gas (Ar(89 %), CO_2(10 %) and CH_4(1 %)) at an atmospheric pressure and is operated at high voltages of 2.00, 2.05, and 2.10 kV for Ring 1, Ring 2 and Rings 3-29, respectively, during the period of data taking.

In order to minimize the material thickness of CDC, carbon-fiber-reinforced plastic(CFRP) which is mechanically strong but has long radiation and interaction lengths, was chosen as that of cylinder. The thicknesses of the inner and outer walls are 1.5 mm and 5.0 mm, respectively. The thicknesses in the direction of $\theta = 90^\circ$ of the inner wall and tracking volume are 0.007 X_0 and 0.0015 X_0, respectively. The end plates are made of 2 cm thick aluminum.

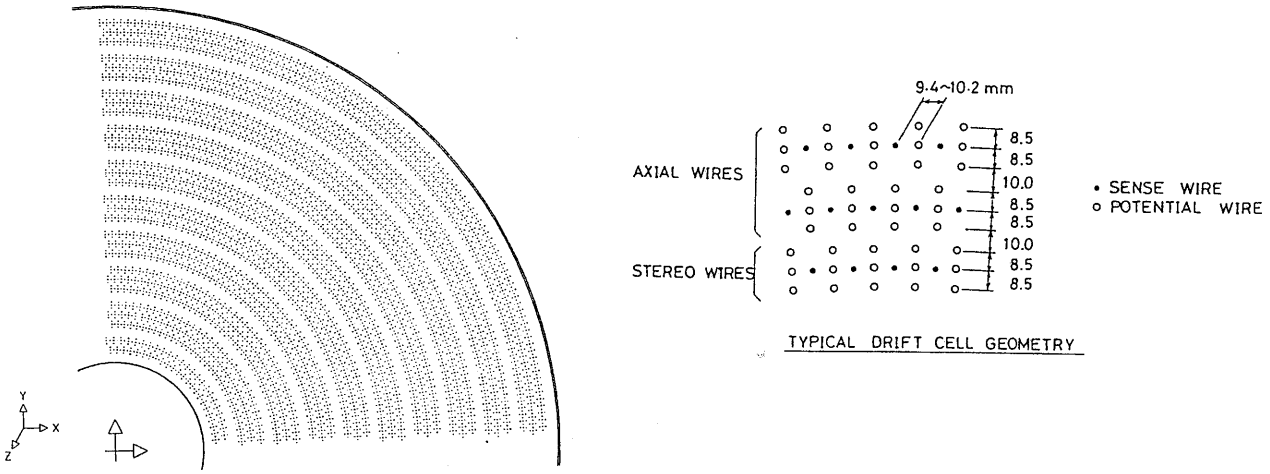

Figure 4.5: The central drift chamber: quadrant part of an end view(left) and wire arrangement(right).

The dimension of the CDC is 300 cm in length with the inner radius of 25 cm and the outer radius of 126 cm. It consists of 7104 single-hit drift cells whose cross sections are about 2×2 cm^2. A unit cell has one anode wire, a gold plated tungsten wire with the diameter of 30 μm, and six cathode wires, gold-plated molybdenum wires with the diameter of 140 μm, as shown in Figure 4.5. There are twenty layers of axial wires parallel to the beam axis to measure the r-ϕ coordinates and nine layers of stereo wires which are slanted with an angle of $\pm3.5°$ with respect to the beam axis to measure the z-coordinate of a track. As shown in Figure 4.5, two adjacent layers of axial wires are staggered by a half cell width. These 29 layers cover the polar angle range of $|\cos\theta| \leq 0.75$. The chamber is filled with HRS gas (Ar(89 %), CO_2(10 %) and CH_4(1 %)) at an atmospheric pressure and is operated at high voltages of 2.00, 2.05, and 2.10 kV for Ring 1, Ring 2 and Rings 3-29, respectively, during the period of data taking.

In order to minimize the material thickness of CDC, carbon-fiber-reinforced plastic(CFRP) which is mechanically strong but has long radiation and interaction lengths, was chosen as that of cylinder. The thicknesses of the inner and outer walls are 1.5 mm and 5.0 mm, respectively. The thicknesses in the direction of $\theta = 90°$ of the inner wall and tracking volume are 0.007 X_0 and 0.0015 X_0, respectively. The end plates are made of 2 cm thick aluminum.

Signals from anode wires are amplified by preamplifiers located on the end plates and sent to post-amplifier-discriminators in the electronics hut. FASTBUS[1] TDC's[2] are used to digitize the drift time. The signals from the discriminators are also fed to a fast track-finder module (TFM) on FASTBUS and used to generate a fast r-ϕ track trigger signal with a look-up table method[25]. Here, TFM is a module to find tracks in CDC during data acquisition and generates triggers. Tracks within a polar angle range of $|\cos\theta| \leq 0.87$ and with transverse momenta of larger than 0.7 GeV/c are detected by the TFM with the detection efficiency of more than 99 %. For charged tracks in the range of $|\cos\theta| \leq 0.75$, the mean spatial resolution is measured to be 270 μm at each axial layer.

4.2.3 Barrel Lead glass Calorimeter

The barrel lead glass calorimeter(LG) [26] is a homogeneous calorimeter used for detection of electromagnetic particles such as electrons and photons. It is located between the solenoid coil and iron return yoke with the radial range of 197-230 cm and length of 615 cm. It covers a range of angle $|\cos\theta| \leq 0.80$. Energies are measured with Čherenkov lights ($\sim 10^3$ photoelectrons for a 1 GeV electron) which are radiated by charged particles in electromagnetic showers. Such a high energy shower develops by the successive bremsstrahlung and e^+e^- pair creation by photons until their energies reach the critical energy. Below the critical energy, ionization by collision processes dominates. So the total amount of the light yield is proportional to the energy deposit in LG modules. The relation between the energy and the light yield was calibrated by using the electron beam from the internal target beam line (IT4) at the AR of the TRISTAN.

The LG calorimeter consists of 5160 lead glass Čherenkov counters and is segmented into 120 blocks in the ϕ-direction and 43 blocks in the z-direction. A lead glass block is made of DF6 whose main components are PbO (70.9 %) and SiO_2(27.3 %), and has properties such as the radiation length of 1.69 cm, the critical energy of 12.6 MeV and the refractive index of 1.805. The typical size is 12.0$\times$11.6 cm^2 in cross section and 30cm in length, corresponding to 18.0 X_0. The lead-glass blocks are pointed to the interaction region to minimize multi-hit probability of the particles. The LG calorimeter is divided into seven sections in the z-direction, and the lead-glass blocks are set parallel within each section as shown in Figure 4.6.

In this configuration, the lead-glass blocks are tilted by 0° to 14° with respect to the line directing to the interaction point. In the r-ϕ plane, all the lead-glass blocks are tilted

[1]FASTBUS is one of the standards of very high performance buses to connect peripherals to the computer.

[2]TDC is time-to-digital converter which converts a time information to a digital number.

Figure 4.6: The lead-glass calorimeter.

by 3° with respect to the radial line. This semi-tower geometry prevents photons from escaping through gaps between blocks. The schematic view of a lead-glass module is shown in Figure 4.7.

A 3-inch diameter photomultiplier tube(PMT) surrounded by a μ-metal magnetic shield is attached to each lead glass block together with a plastic light guide of 5 cm in length. At the central part of the LG calorimeter, box- and grid-type of PMTs are used, while at both end parts where the leakage field is 20 to 30 Gauss, mesh-type PMT are used. High voltages ranging from -1.5 to -2.0 kV are applied to PMTs during data taking.

Signals from PMTs are sent to 96 channel 12-bit charge integrating ADC[3] modules on FASTBUS. For the energy trigger, the LG calorimeter is divided into 58 segments i.e. seven segments in the z-direction and eight or ten segments in the ϕ direction. Each ADC module corresponding to one segment produces an analog segment-sum signal. Each of 58 segment-sum signals is sent to a discriminator and its output signal is used for the segment-sum trigger. Also all 58 segment-sum signals are sent to an analog-sum circuit to obtain the total energy deposit which is used for the total-energy trigger. In order to trace gain fluctuation of the PMTs, a monitoring system which is made of a Xe flash tube with optical fibers is used.

[3]ADC is analog-to-digital converter which converts an analog information to a digital number.

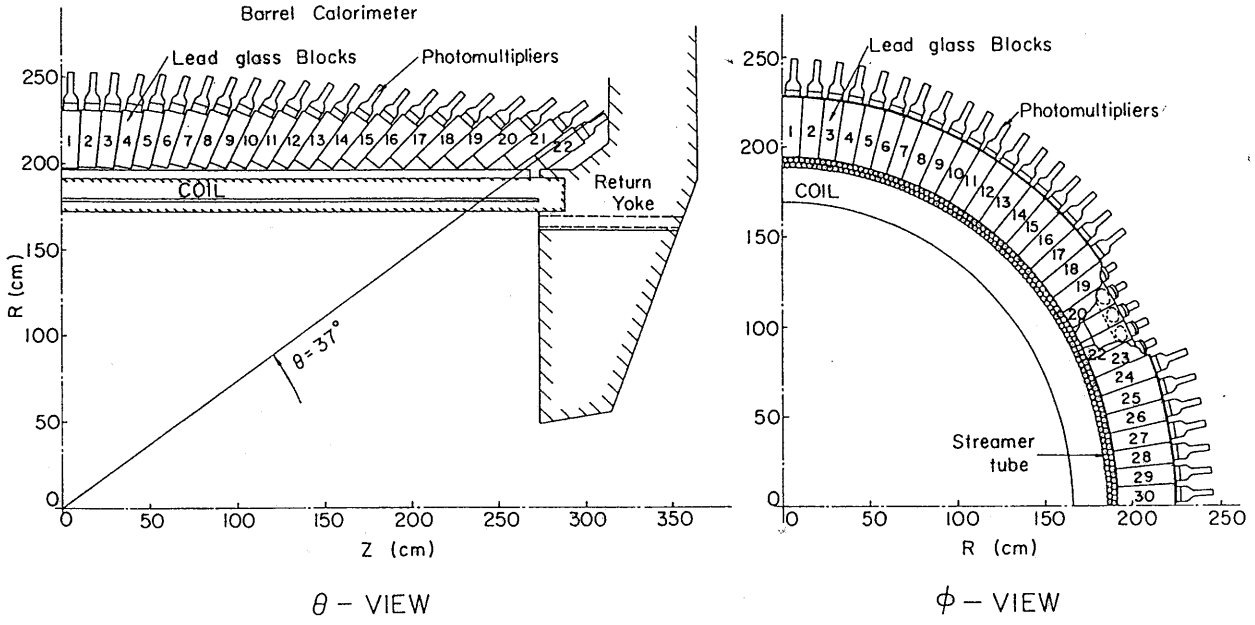

Figure 4.6: The lead-glass calorimeter.

by 3° with respect to the radial line. This semi-tower geometry prevents photons from escaping through gaps between blocks. The schematic view of a lead-glass module is shown in Figure 4.7.

A 3-inch diameter photomultiplier tube(PMT) surrounded by a μ-metal magnetic shield is attached to each lead glass block together with a plastic light guide of 5 cm in length. At the central part of the LG calorimeter, box- and grid-type of PMTs are used, while at both end parts where the leakage field is 20 to 30 Gauss, mesh-type PMT are used. High voltages ranging from -1.5 to -2.0 kV are applied to PMTs during data taking.

Signals from PMTs are sent to 96 channel 12-bit charge integrating ADC[3] modules on FASTBUS. For the energy trigger, the LG calorimeter is divided into 58 segments i.e. seven segments in the z-direction and eight or ten segments in the ϕ direction. Each ADC module corresponding to one segment produces an analog segment-sum signal. Each of 58 segment-sum signals is sent to a discriminator and its output signal is used for the segment-sum trigger. Also all 58 segment-sum signals are sent to an analog-sum circuit to obtain the total energy deposit which is used for the total-energy trigger. In order to trace gain fluctuation of the PMTs, a monitoring system which is made of a Xe flash tube with optical fibers is used.

[3]ADC is analog-to-digital converter which converts an analog information to a digital number.

Figure 4.7: Assembly of a lead-glass module.

4.2.4 End-cap liquid argon calorimeter

The end-cap liquid argon calorimeter(LA) is a sampling calorimeter for measuring the energies of electromagnetic particles in the forward and backward region[29]. The energies are measured by collecting charges from the ionization by the shower particles. Two liquid argon calorimeters are installed between the CDC and both end-caps of the return yoke. Each one covers an angular range of $0.79 \leq |\cos\theta| \leq 0.99$ as shown in Figure 4.8. Each calorimeter consists of 480 tower structure modules which, look at the point 80 cm away from the interaction point on the beam axis(semi-tower geometry). A schematic view of LA is shown in Figure 4.8. Each tower module consists of 71 calcium-lead plates of 1.5 mm thick which corresponds to 20.3 radiation lengths. The whole calorimeters are filled with liquid argon of 86 K. Lead plates of each tower are electrically segmented into four groups, so each side of the calorimeter has 1920 channels of signal read-out. Signals are amplified by preamplifiers on the outer vessel of each calorimeter and sent to shaper-amplifiers. Pulse heights are measured by sample-hold analog-to-digital converters(ADC) on TKO interface boxes[29].

Tow types of energy-sum triggers are provided using the analog-sum circuits for LA. Each calorimeter is divided into 12 sectors and each sector is further divided into the inner($0.91 \leq |\cos\theta| \leq 0.99$) and the outer($0.79 \leq |\cos\theta| \leq 0.91$) part. Thus energy-sum signals from the 48 sub-sectors in both sides are used for the sector-sum trigger. Furthermore, the total-sum signal of all 1920 channels for each side is used for the forward-(or backward-) sum trigger.

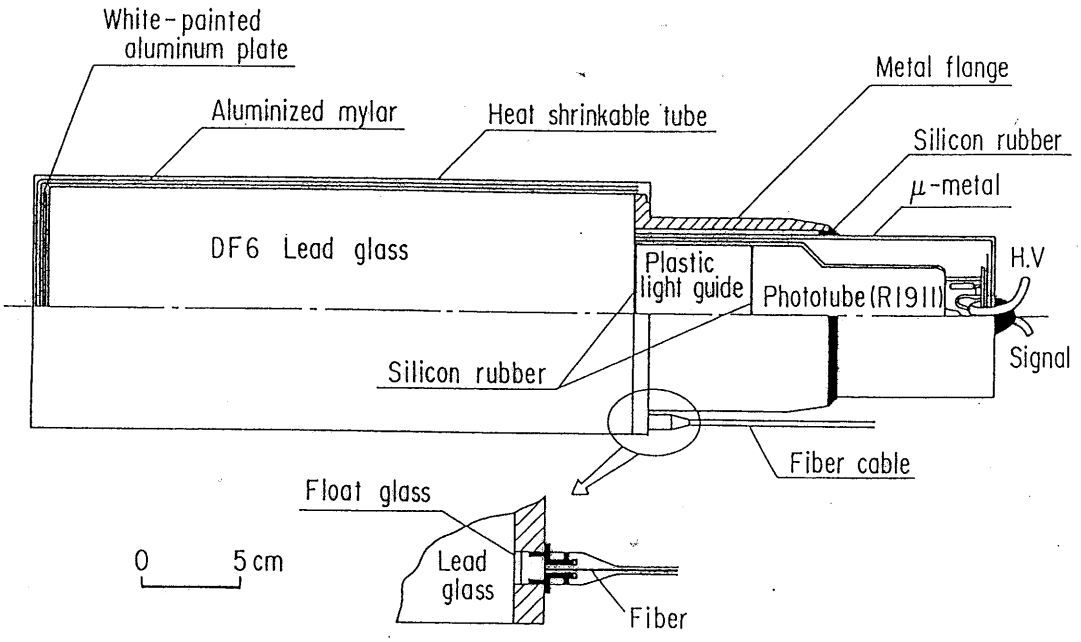

Figure 4.7: Assembly of a lead-glass module.

4.2.4 End-cap liquid argon calorimeter

The end-cap liquid argon calorimeter(LA) is a sampling calorimeter for measuring the energies of electromagnetic particles in the forward and backward region[29]. The energies are measured by collecting charges from the ionization by the shower particles. Two liquid argon calorimeters are installed between the CDC and both end-caps of the return yoke. Each one covers an angular range of $0.79 \leq |\cos\theta| \leq 0.99$ as shown in Figure 4.8. Each calorimeter consists of 480 tower structure modules which, look at the point 80 cm away from the interaction point on the beam axis(semi-tower geometry). A schematic view of LA is shown in Figure 4.8. Each tower module consists of 71 calcium-lead plates of 1.5 mm thick which corresponds to 20.3 radiation lengths. The whole calorimeters are filled with liquid argon of 86 K. Lead plates of each tower are electrically segmented into four groups, so each side of the calorimeter has 1920 channels of signal read-out. Signals are amplified by preamplifiers on the outer vessel of each calorimeter and sent to shaper-amplifiers. Pulse heights are measured by sample-hold analog-to-digital converters(ADC) on TKO interface boxes[29].

Tow types of energy-sum triggers are provided using the analog-sum circuits for LA. Each calorimeter is divided into 12 sectors and each sector is further divided into the inner($0.91 \leq |\cos\theta| \leq 0.99$) and the outer($0.79 \leq |\cos\theta| \leq 0.91$) part. Thus energy-sum signals from the 48 sub-sectors in both sides are used for the sector-sum trigger. Furthermore, the total-sum signal of all 1920 channels for each side is used for the forward-(or backward-) sum trigger.

Figure 4.8: The liquid argon calorimeter: (a) end view and (b) sectional view.

4.2.5 Time-of-flight Counter

The time-of-flight(TOF) counter system is used for triggering and identification of the species of detected particles by accurately measuring their flight time [27]. Figure 4.9 shows a schematic view of the TOF counter system. The TOF counter system consists of 96 plastic scintillators with a dimension of $4.2\times10.8\times466$ cm^3. These counters are fixed on the inner wall of the superconducting solenoid at the radius of 166 cm from the beam axis and cover the range of $|\cos\theta| \leq 0.81$. There are 3 mm gaps between two adjacent counters. These gaps cause the inefficiency of about 3 %. Each end of scintillator is viewed by a PMT through a 145 cm long acrylic light guide.

Signals from PMTs are transmitted to discriminators and the TDC-ADC system in the TKO[4] box. Output signals from the discriminators are also used for an event trigger. The time resolution was estimated to be about 200 psec by using Bhabha and μ-pair events.

[4]TKO is one of the standards of buses developed at KEK to connect peripherals to the computer.

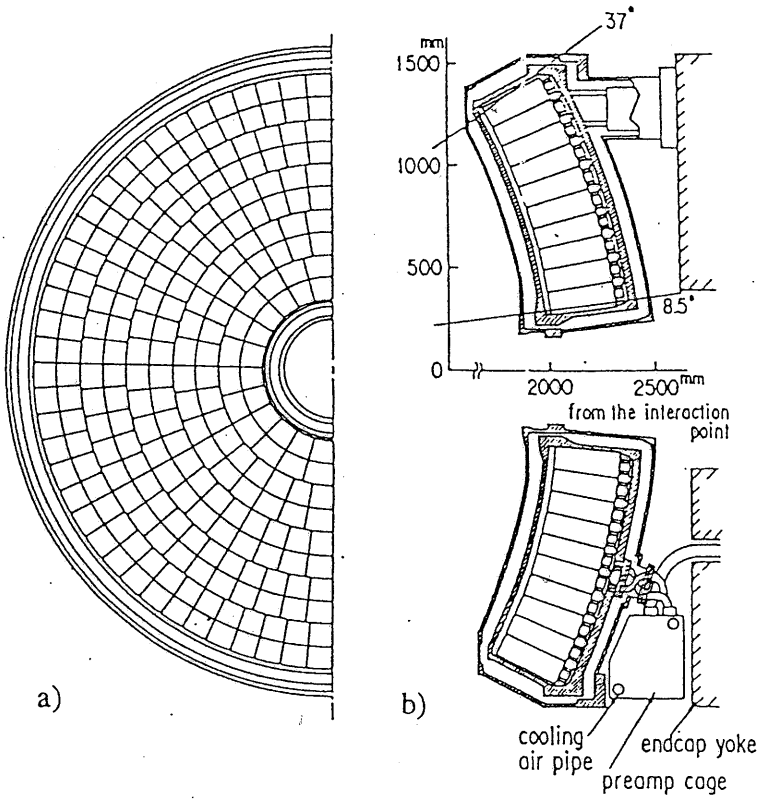

Figure 4.8: The liquid argon calorimeter: (a) end view and (b) sectional view.

4.2.5 Time-of-flight Counter

The time-of-flight(TOF) counter system is used for triggering and identification of the species of detected particles by accurately measuring their flight time [27]. Figure 4.9 shows a schematic view of the TOF counter system. The TOF counter system consists of 96 plastic scintillators with a dimension of $4.2\times10.8\times466$ cm^3. These counters are fixed on the inner wall of the superconducting solenoid at the radius of 166 cm from the beam axis and cover the range of $|\cos\theta| \leq 0.81$. There are 3 mm gaps between two adjacent counters. These gaps cause the inefficiency of about 3 %. Each end of scintillator is viewed by a PMT through a 145 cm long acrylic light guide.

Signals from PMTs are transmitted to discriminators and the TDC-ADC system in the TKO[4] box. Output signals from the discriminators are also used for an event trigger. The time resolution was estimated to be about 200 psec by using Bhabha and μ-pair events.

[4]TKO is one of the standards of buses developed at KEK to connect peripherals to the computer.

Figure 4.9: The time-of-flight counter system.

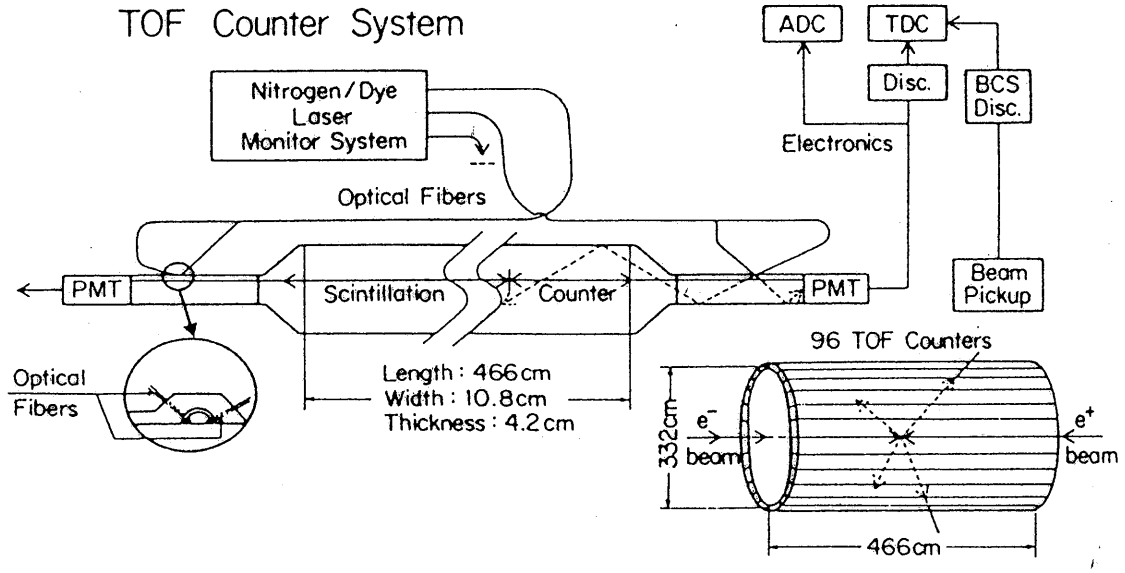

Figure 4.9: The time-of-flight counter system.

4.2.6 Transition Radiation Detector

Transition Radiation

When an ultra-relativistic charged particle of Lorentz factor $\gamma \geq O(1000)(\gamma = 1/\sqrt{1-\beta^2})$ traverses two media which are attached to each other and have different dielectric constants, an X-ray called "transition radiation" is produced at the boundary. Total energy of the radiation is given as

$$S = \frac{\alpha}{3}\frac{(\omega_1 - \omega_2)^2}{\omega_1 + \omega_2}\gamma \qquad \simeq \frac{\alpha}{3}\gamma\omega_1 \text{ (for } \omega_1 \gg \omega_2), \tag{4.5}$$

where $\omega_{1,2}$ are plasma frequencies of the media and α is the fine structure constant($= 1/137$). Apparently total energy of the transition radiation is found to be proportional to Lorentz factor γ from Eq.(4.5).

TRD in VENUS detector

TRD is a large cylindrical transition radiation detector, extending from 127 cm to 157.7 cm radially and 296 cm in z direction[22] as shown in Figure 4.10. It is designed to improve e/π separation capability. It covers the angular region of $|\cos\theta| \leq 0.68$ and composed of two parts. One is an airtight "radiator box" which contains radiative material and helium gas and the other is a X-ray chamber filled with xenon gas to detect the transition radiation. TRD is divided into eight octants; each has four layers of the radiator box and X-ray chamber pair. Thus 32 pairs of radiator box and X-ray chamber compose the detector. The whole structure is composed of a pair of endplates(of 15 mm thick aluminum), inner and outer cylinder(of 3 mm thick aluminum) and eight side-panels. The side panels, which separate octants, consist of 13.8 mm thick aluminum honeycomb with 0.6 mm aluminum skin on each side. There are windows that separate radiators from chambers. The X-ray chambers are composed of an aluminized mylar sheet as the window on inner surface and an aluminum plate on the outer surface to separate itself from the neighboring radiator. In the middle, anode wires are strung along z axis between two endplates. The total radiation length of TRD is $0.18X_0$.

The X-ray chamber is a 2 cm thick drift chamber with 2688 sense wires, which operates in xenon/methane gas at 15±10 mm water above atmospheric pressure. It has been working very stably since it started data-taking in June 1991. The pion rejection power ($R_\pi = 1/\epsilon_\pi$) at an electron efficiency of 90 % is $R_\pi \sim 10$ and ~ 15 for isolated tracks within momentum ranges of $1 < p < 3$ and $3 < p < 10$ GeV/c, respectively. It decreases to $R_\pi \sim 7$ for tracks with $p < 1$ GeV/c in hadronic events due to overlap of the chamber cells of the TRD.

Figure 4.10: Over View of TRD

4.2.7 Muon Detector

The muon detector system covers the large outermost area of the VENUS detector to detect penetrating tracks [28]. It consists of two main parts: the barrel part and the

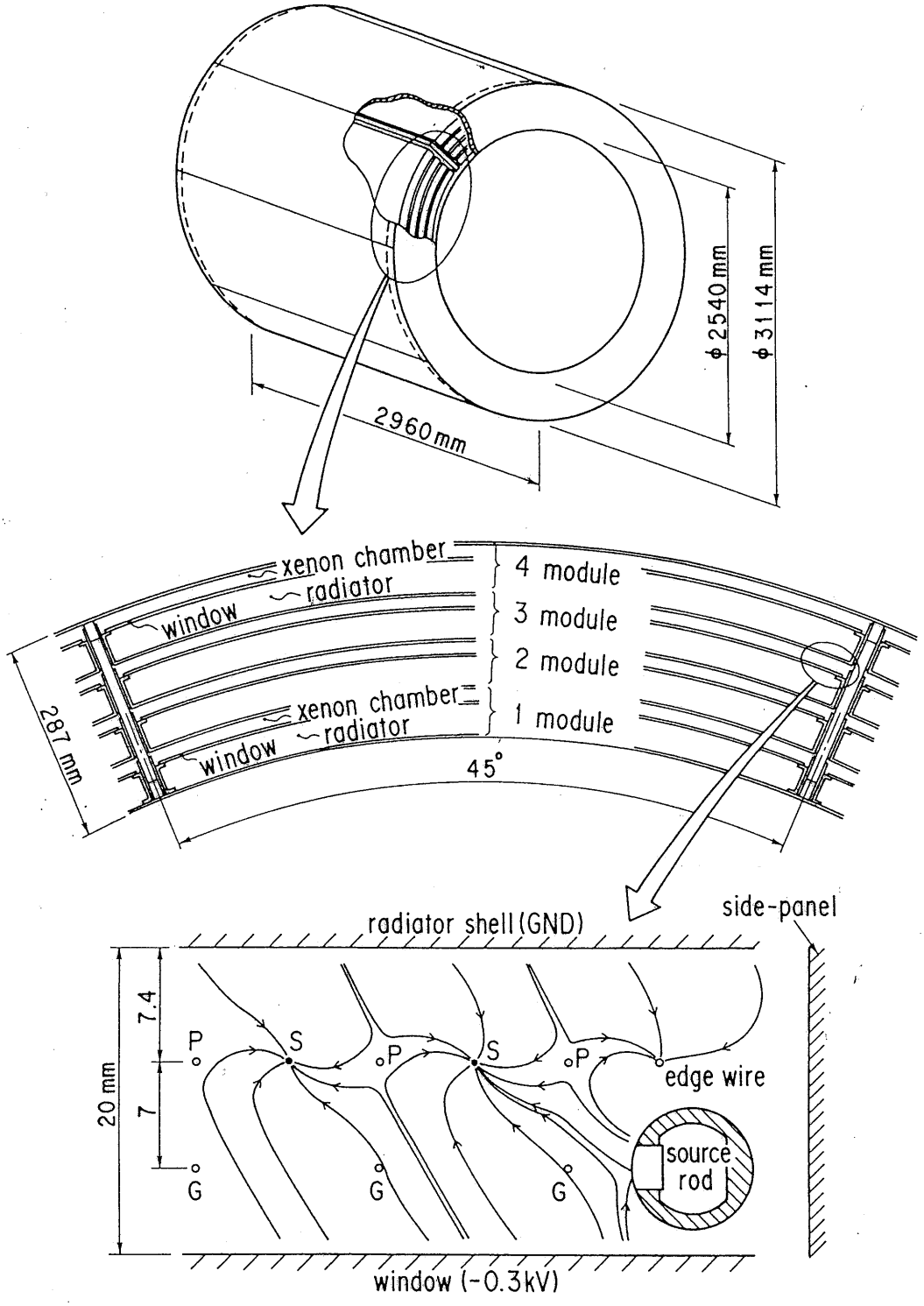

Figure 4.10: Over View of TRD

4.2.7 Muon Detector

The muon detector system covers the large outermost area of the VENUS detector to detect penetrating tracks [28]. It consists of two main parts: the barrel part and the

forward-backward part. Both parts consist of four layered array of extruded aluminum modules, each with eight cells of drift tubes. A module consists of two layers of four cells staggered by a half cell as shown in Figure 4.11.

Figure 4.11: A module of muon chamber.

Each cell has a cross section of 5×7 cm^2 with the wall thickness of 2.5 mm on average. Lengths of the modules are 760 cm for the barrel part, and vary from 245 cm to 505 cm depending on the location for the forward-backward part. The sense wire of 70 μm in diameter made of gold-plated tungsten with 3 % rhenium is stretched at the center of each cell with a tension of 400 g. The tubes are filled with P-10 gas (Ar:CH_4 = 90:10). High voltage of 2.7 kV is applied to each sense wire and the tubes are operated in a proportional mode.

In the barrel part, inner three layers of the modules, interleaved with 20 cm thick iron filters, measure the r-ϕ positions of the penetrating track. The outermost layer, which is located just outside of the third layer without any iron filters between them, measures the z-position of the track. In the forward-backward part, four layers of modules are placed alternately to measure z-x and z-y positions.

Signals from anode wires are amplified and digitized by the front-end electronics boards which are mounted at one end of each tube. Digitized data are sent to memory boards on TKO boxes in the electronics hut together with the wire address information.

In the barrel region, the main absorbing material consists of the lead glass calorimeter,

forward-backward part. Both parts consist of four layered array of extruded aluminum modules, each with eight cells of drift tubes. A module consists of two layers of four cells staggered by a half cell as shown in Figure 4.11.

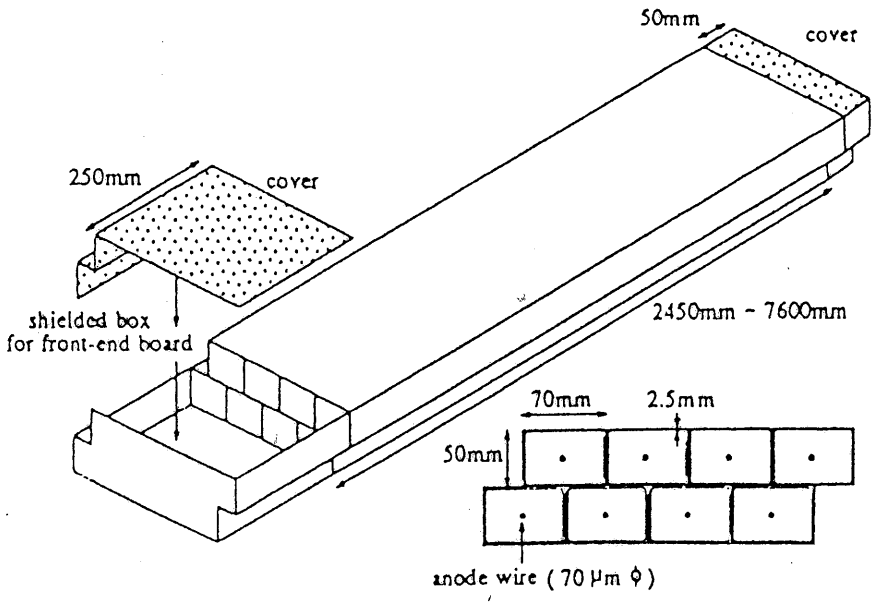

Figure 4.11: A module of muon chamber.

Each cell has a cross section of 5×7 cm^2 with the wall thickness of 2.5 mm on average. Lengths of the modules are 760 cm for the barrel part, and vary from 245 cm to 505 cm depending on the location for the forward-backward part. The sense wire of 70 μm in diameter made of gold-plated tungsten with 3 % rhenium is stretched at the center of each cell with a tension of 400 g. The tubes are filled with P-10 gas (Ar:CH_4 = 90:10). High voltage of 2.7 kV is applied to each sense wire and the tubes are operated in a proportional mode.

In the barrel part, inner three layers of the modules, interleaved with 20 cm thick iron filters, measure the r-ϕ positions of the penetrating track. The outermost layer, which is located just outside of the third layer without any iron filters between them, measures the z-position of the track. In the forward-backward part, four layers of modules are placed alternately to measure z-x and z-y positions.

Signals from anode wires are amplified and digitized by the front-end electronics boards which are mounted at one end of each tube. Digitized data are sent to memory boards on TKO boxes in the electronics hut together with the wire address information.

In the barrel region, the main absorbing material consists of the lead glass calorimeter,

their support rings made of 17.5 cm thick iron and 10.0 cm thick aluminum, the return yoke made of 30.0 cm thick iron and two muon filters, each comprising 20.0 cm thick iron. Thickness of each muon filter is chosen to be about one absorption length of hadrons. Distances between the return yoke and the first muon filter and between the first and the second muon filter are chosen to be both 15.0 cm to minimize possible decays of surviving pions and kaons. Particles should penetrate at least 4.3 absorption lengths of material to reach the first layer of the muon chamber and additional one or two absorption lengths of material to reach the second or third layer.

4.2.8 Magnet

The VENUS magnet system consists of a superconducting solenoid, a flux return yoke, a helium refrigerator and a high current power supply [30]. The superconducting solenoidal coil has its dimension of 177 cm in radius and 527 cm in length. It provides a uniform magnetic field of 7.5 kG in the longitudinal direction. Its superconducting material is Nb-Ti/Cu. The excitation current is approximately 4000 A at 7.5 kG. The material thickness of the solenoid is made exceedingly thin, 0.52 X_0.

The iron return yoke supports the magnetic force of about 230 t with a maximum elastic deformation of 0.4 mm. The cryogenic system keeps the temperature of the solenoid below 4.5 K. The stored energy is estimated to be 11.7 MJ.

The magnetic field in a volume of 3.2 m diameter by 4 m length was measured by using a nuclear-magnetic resonance (NMR) probe for the absolute value and Hall probes for the three dimensional components with the accuracy of order of 10^{-4}. The uniform field of 7.5 kG was obtained in the CDC region within a deviation of 0.3 %.

4.3 Event Trigger and Data Acquisition System

4.3.1 Trigger System

The VENUS trigger system [34] is composed of two levels: a first-level trigger designed to work between beam crossings and a second-level trigger which uses software and is slower. Furthermore, the first-level trigger is classified into two types: a neutral trigger based on the information of high energy deposit in any of electromagnetic calorimeters and a charged track trigger based on the information of the CDC. Their signals are processed by a trigger decision module(TDM). The decision is made within a collision interval of 5 μsec. In the second-level trigger, a 68K20FPI microprocessor accepts an event when it satisfies severer conditions than those of the first-level trigger.

Trigger	Condition
Coplanar trigger	(2 CDC charged tracks)×(2 TOF hits)
LG segment sum	(E≥0.7 GeV)×(2 CDC charged tracks)
LG total sum	E≥3 GeV
LA total sum	E≥4 GeV
LA sector sum	E≥2 GeV
Luminosity trigger	E≥10 GeV
Random trigger	0.1 Hz

Table 4.2: The first level triggers.

The trigger conditions during the data taking are as follows:

- Charged track trigger

  1. Coplanar trigger
     At least one pair of tracks with transverse momenta to the beam axis larger than 0.7 GeV/c in a back-to-back configuration is found by TFM. The acoplanarity angle between two tracks must be less than 10°. Here, the acoplanarity angle is defined as the supplementary angle in the r-ϕ plane between the two tracks and expressed as
     $$\theta_{\rm acop} = \cos^{-1}\left(\frac{-p_{t1}\cdot p_{t2}}{|p_{t1}||p_{t2}|}\right),$$
     where p_{t1} and p_{t2} are the momentum vectors projected on to the r-ϕ plane.
  2. LG segment sum trigger
     At least two tracks with p_t larger than 0.7 GeV/c are found and it is required that at least one of LG segments has an energy deposit larger than 0.7 GeV.

- Neutral trigger

  1. LG total sum trigger
     A total energy deposit in LG is larger than 3 GeV.
  2. LA total sum trigger
     At least one side of LA has a total energy deposit larger than 4 GeV.
  3. LA sector sum trigger
     At least one of the sectors in LA has an energy deposit larger than 2 GeV.

4. Luminosity trigger
   LM(luminosity monitor) should have energy deposits larger than 10 GeV in a back-to-back configuration. This trigger is provided for Bhabha events in the small polar angle region to make on-line monitoring of the luminosity.

The above first-level trigger conditions are listed in Table 4.2. In addition to these six triggers, a random trigger is made at every 10 sec to monitor accidental background.

Figure 4.12 shows a block diagram of the first-level trigger logic. The acceptance of

Figure 4.12: Block diagram of the trigger logic. MALU is CAMAC majority logic unit to count the multiplicity of tracks. SR is one of FASTBUS signals to interrupt the on-line computer and mask the subsequent signals if the trigger condition is satisfied.

the coplanar trigger is extended to $\theta_{\rm acop} \leq 25^\circ$ at present. The coplanar-triggered events contain a large number of backgrounds which amount to about a half of all the events. The second-level trigger is a software trigger with a 68K20FPI which processes information of the TFM and TOF. It reduces the number of the coplanar-triggered events to about 50 % by using severer track finding conditions. The total trigger rates is typically $5 \sim 7$ Hz though it strongly depends on the beam condition.

4.3.2 Data Acquisition System

The VENUS data acquisition system [35] has a tree-like structure as shown in Figure 4.13. For the front-end electronics, several data buses such as CAMAC, TKO, and FASTBUS are used. These buses handle about 30000 electronic readout channels in total.

4. Luminosity trigger

   LM(luminosity monitor) should have energy deposits larger than 10 GeV in a back-to-back configuration. This trigger is provided for Bhabha events in the small polar angle region to make on-line monitoring of the luminosity.

The above first-level trigger conditions are listed in Table 4.2. In addition to these six triggers, a random trigger is made at every 10 sec to monitor accidental background.

Figure 4.12 shows a block diagram of the first-level trigger logic. The acceptance of

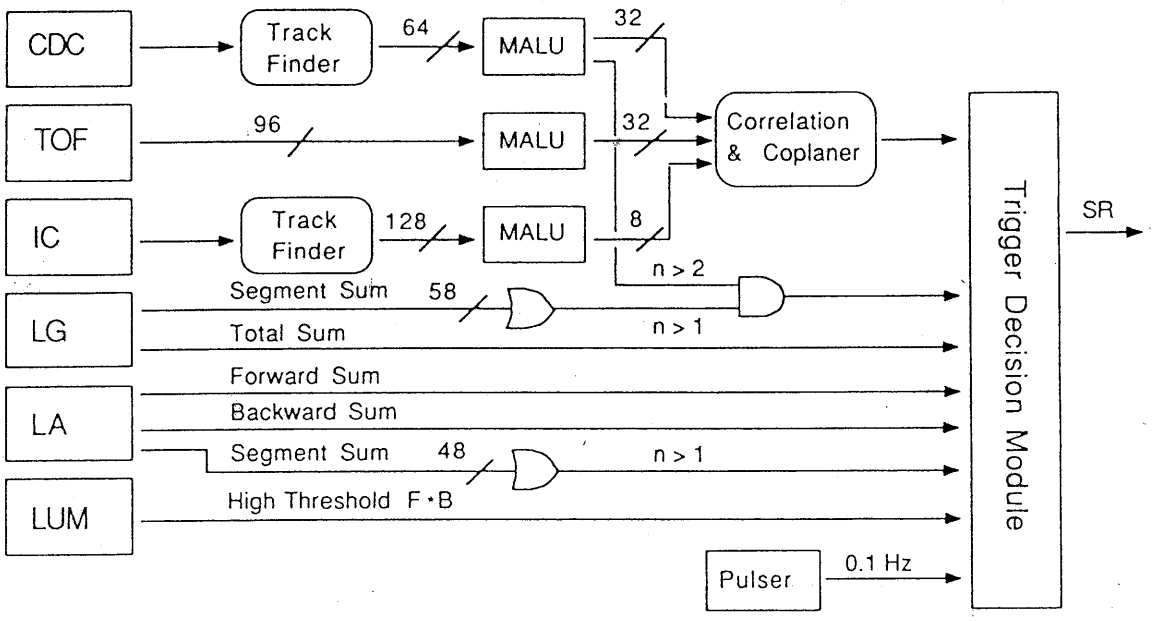

Figure 4.12: Block diagram of the trigger logic. MALU is CAMAC majority logic unit to count the multiplicity of tracks. SR is one of FASTBUS signals to interrupt the on-line computer and mask the subsequent signals if the trigger condition is satisfied.

the coplanar trigger is extended to $\theta_{\rm acop} \leq 25°$ at present. The coplanar-triggered events contain a large number of backgrounds which amount to about a half of all the events. The second-level trigger is a software trigger with a 68K20FPI which processes information of the TFM and TOF. It reduces the number of the coplanar-triggered events to about 50 % by using severer track finding conditions. The total trigger rates is typically $5 \sim 7$ Hz though it strongly depends on the beam condition.

4.3.2 Data Acquisition System

The VENUS data acquisition system [35] has a tree-like structure as shown in Figure 4.13. For the front-end electronics, several data buses such as CAMAC, TKO, and FASTBUS are used. These buses handle about 30000 electronic readout channels in total.

All digitized data from the front-end electronics of the detector components are transferred to FASTBUS memory buffers and collected by a 68K20FPI module on FASTBUS whenever an event trigger occurs. And then all the data in 68K20FPI are read by an on-line computer VAX6320 through the FASTBUS-VAX interface.

The collected data are sent to the main frame computer FACOM M1800 via optical fibers and then stored in an automatic loading cartridge tape library.

Figure 4.13: VENUS data acquisition system. Abbreviated module names are as follows; 68K - 68000 FASTBUS processor interface, CAT - calibration and trigger module, CH - control head, FCI - FASTBUS-CAMAC interface, IOR - input/output register, MAL - majority logic, MP - memory partner, MRB - multirecord buffer, SADC - scanning ADC, SMI - segment manager interface, SOI - segment optical isolator, SSI - simplex segment interconnect, STOS - streamer tube operating system, TAC - 64ch time-to-amplitude converter, TFC - track finder for CDC, TFI - track finder for inner chamber, (A)T - cable segment(active) terminator.

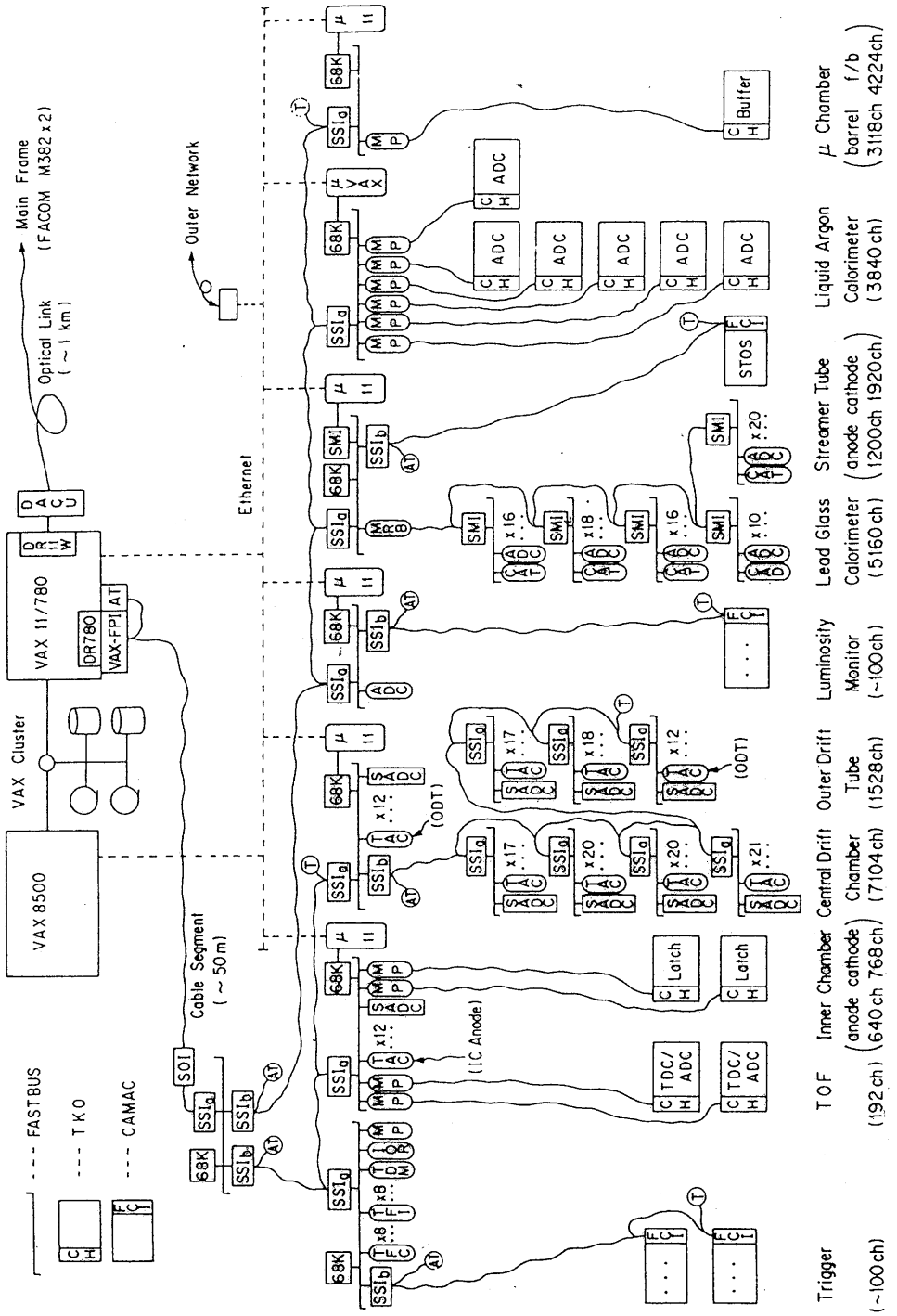

Figure 4.13: VENUS data acquisition system. Abbreviated module names are as follows; 68K - 68000 FASTBUS processor interface, CAT - calibration and trigger module, CH - control head, FCI - FASTBUS-CAMAC interface, IOR - input/output register, MAL - majority logic, MP - memory partner, MRB - multirecord buffer, SADC - scanning ADC, SMI - segment manager interface, SOI - segment optical isolator, SSI - simplex segment interconnect, STOS - streamer tube operating system, TAC - 64ch time-to-amplitude converter, TFC - track finder for CDC, TFI - track finder for inner chamber, (A)T - cable segment(active) terminator.

Chapter 5

Event Reconstruction

The informations needed in the present analysis are given by charged tracks in the CDC, electromagnetic showers in the LG and LA calorimeters, energy deposits in TRD and the muon chamber hits. The event reconstruction is made in two steps. At first, raw data are processed through the calibration routines in which the digitized data are converted into physical quantities *i.e.* drift lengths for CDC tracks and energy deposits for LG or LA showers. Next, the calibrated data are processed by such routines as to reconstruct CDC-tracks and LG or LA energy clusters.

The outline of this second step and the procedure of analysis routines are described below.

5.1 CDC Track Reconstruction

The momentum measurement and charge sign determination of a charged particle are performed by reconstructing its trajectory in the CDC. Since a magnetic field of 7.5 kG is applied along the z-axis, the charged particle trajectory spirals in the three-dimensional space and thus makes a circle when projected onto the r-ϕ plane. The transverse momentum p_t (GeV/c) can be obtained from the relation

$$p_t = 0.3 \cdot B \cdot \rho, \tag{5.1}$$

where B is the magnetic flux density in Tesla, and ρ is the radius of curvature in meter. In this analysis, the distance of the closest approach to the interaction point in the r-ϕ plane is defined as R_{min}. We define R_{min} to be positive if the interaction point lies within the circle of a track and otherwise to be negative. This configuration is illustrated in Figure 5.1. The track reconstruction in the CDC is carried out by using the pattern recognition program named PERPR[36]. The basic procedure of the track reconstruction in PERPR is described below.

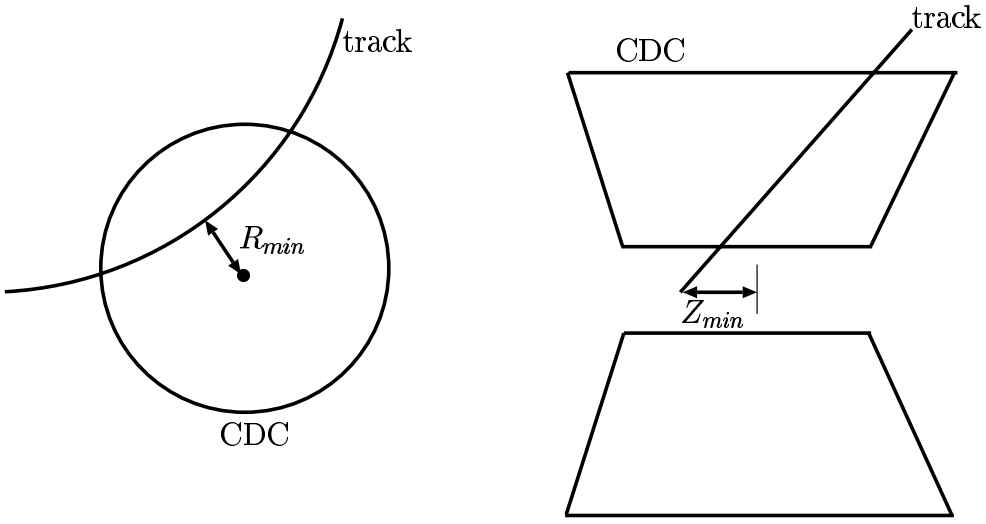

Figure 5.1: Definition of track parameters: (a) R_{min} and (b) Z_{min}.

Reconstruction in the r-ϕ plane

The track reconstruction in the r-ϕ plane is performed as follows,

1. The "initial road" is searched at the most outer two layers of the CDC. If the double layer hits (successive hits in the two layers) are found, the "road" of a track is defined. Thus, four possible combinations of a track due to left-right ambiguity are taken into account.

2. The candidate hits along the "road" are searched. To find the most likely track, the least χ^2 fit is performed by eliminating hits of poor quality. If χ^2 exceeds 5.0, the track is abandoned.

3. The curvature of the track is calculated from the above formula and relevant quantities such as charge, p_t, and R_{min} are calculated.

Reconstruction in the r-z plane

The slant-layer hits are used in association with the axial-layer hits to determine the three-dimensional trajectory. Since the slant wires are inclined by 3.5 degrees with respect to the axial wires, the z-coordinate of the track can be given by

$$z = \frac{\ell}{2} - \frac{d}{\tan\alpha}, \tag{5.2}$$

where d is the distance between the axial track and the stereo hit(Figure 4.5), α is the slant angle (3.5 degrees) and ℓ is the wire length of the slant wire projected onto the beam axis. The overall trajectory can be expressed in the linear from as

$$z = \frac{dz}{ds}s + Z_{min}, \tag{5.3}$$

where Z_{min} is the distance at the closest approach in the r-z plane, s is the length of arc element and dz/ds is the gradient. The track finding algorithm of the PERPR is similar to that for the r-ϕ plane.

Tracking performance

For charged tracks in the range of $|\cos\theta| \leq 0.75$ where they are able to pass through all axial and slant layers of CDC, the tracking performance has been evaluated using Bhabha scattering events. The vertex resolutions for high-p_t tracks have been found to be

$$\sigma_{vtx}(r-\phi) \simeq 460\ \mu m,$$
$$\sigma_{vtx}(z) \simeq\ 6.7mm.$$

In the same way, the angular resolutions in the azimuthal and polar angles have been estimated to be

$$\sigma_{\theta}^{CDC} = 8\sin^2\theta \text{ mrad},$$
$$\sigma_{\phi}^{CDC} = 1.3 \text{ mrad}$$

The measurement of the polar angle is much less accurate than that for the azimuthal angle. The momentum resolution has been found to be

$$\frac{\sigma_p}{p} = \sqrt{(0.013)^2 + (0.008 \times p_t)^2}, \tag{5.4}$$

with p and p_t in GeV/c in a magnetic field of 7.5 kG using cosmic ray and Bhabha data samples. The first term in Eq.(5.4) is the contribution from multiple coulomb scattering in the materials of the detector; the chamber gas and the wires. The second term is due to the error in the measurement of the drift distance.

The reconstruction efficiency for high-p_t charged tracks in the range of $|\cos\theta| \leq 0.75$ has been studied by collinear Bhabha events and found to be better than 99.9 % in the r-ϕ plane.

5.2 LG Clustering

Since an electromagnetic shower generally spreads over several LG blocks, the shower energy and its incident position should be determined by an appropriate clustering method.

Clustering method

The intrinsic limitations in spatial resolution are firstly given by detector granularity, and secondly by lateral spread of the electromagnetic shower which is mainly caused by

multiple scattering of low-energy electrons that no longer radiate any photons and drift away from the shower center axis. The proper scaling variable for the lateral shower distribution is the *Molière radius* R_M which is given by

$$R_M = \frac{21}{E_c} X_0, \tag{5.5}$$

where E_c is the critical energy for the detector material in MeV and R_M corresponds to 2.8 cm for the lead glass material DF6. Accordingly, several blocks share the shower energy permitting the measurement of the shower center position. The clustering and the measurement of the shower center are performed as follows:

1. Starting from the module which contains the highest energy, the neighboring modules are examined whether they belong to the same cluster or not. Thus, the "connected region" is formed by searching all neighboring modules adjacent in the ϕ or θ direction.
2. The shower energy is calculated by summing up the energies in the same cluster.
3. The incident position of the showering particle is determined by the energy weighted average of the position of the LG blocks in the cluster as follows:

$$x_{cluster} = \frac{\sum_{i=1}^{n} E_i^{\alpha} x_i}{\sum_{i=1}^{n} E_i^{\alpha}}, \tag{5.6}$$

where x_i is the central ϕ- or θ-position of the i-th block in a cluster and $\alpha = 0.34$ which was optimized by a shower simulation calculation using EGS4 program [37].

Performance of LG cluster reconstruction

The energy resolution for an electron is estimated to be

$$\frac{\sigma_E}{E} = 0.025 + \frac{0.07}{\sqrt{E}}, \tag{5.7}$$

where E is in GeV. This was obtained by using $e^+e^- \to e^+e^-, e^+e^-\gamma$ and $e^+e^-e^+e^-$ events. The first term accounts for the systematic error such as instrumental noise, shower leakage and inter-calibration error, whereas the second term is due to the statistical fluctuation of the number of photoelectrons.

The angular resolution of the calorimeter can be studied by comparing the measured shower center position with the CDC track extrapolated to the LG module surface for large angle Bhabha scattering. The angular resolution has been measured to be

$$\sigma_\theta^{LG} = 4.0 \text{ mrad},$$
$$\sigma_\phi^{LG} = 5.2 \text{ mrad}. \tag{5.8}$$

5.3 LA Clustering

Clustering method

The cluster finding algorithm for the LA is similar to that for the LG except that only adjacent towers are included in the search and not for towers in diagonal direction. The center of the cluster is measured by a shower-profile method. It is known that the lateral shower spread $E(x)$ of the electromagnetic shower can be expressed by the following double exponential form [38]:

$$E(x) \cong E_1 \exp(-\frac{|x|}{\lambda_1}) + E_2 \exp(-\frac{|x|}{\lambda_2}), \tag{5.9}$$

where x is the distance from the shower center, and λ_1 and λ_2 represent the shower extension. The first term is the central component which describes the multiple coulomb scattering of the electrons and positrons in the material. The second term is the peripheral component which arises via isotropic propagation of photons. In principle, the shower center can be obtained by solving the above equation but this is generally difficult. To make the problem easier, only one exponential term has been considered. The slope parameter λ has been taken as a function of lateral energy so that

$$\lambda = g(y), \tag{5.10}$$

with

$$y = \ln \frac{1}{2}(\frac{E_i}{E_{i+1}} + 1), \tag{5.11}$$

where E_i represents the energy deposit in the i-th tower. The function $g(y)$ has been parameterized for high-energy electromagnetic showers by using EGS4.

Performance of LA cluster reconstruction

The energy resolution of the LA calorimeter has been studied using radiative Bhabha scattering events, and found to be

$$\frac{\sigma_E}{E} = 1.6\% + \frac{10.2\%}{\sqrt{E}}, \tag{5.12}$$

where E is in GeV. The first term arises from the intrinsic noise, shower leakage and inter-calibration error. The second term is due to the statistical fluctuations of the energy deposition in the liquid argon (Landau fluctuation) and the track-length of the electromagnetic shower. The normalization factor for the energy calibration is given by measuring the energies of Bhabha events.

The angular resolution of the calorimeter has been studied by the same method as that used for the LG calorimeter. It is obtained to be

$$\begin{aligned} \sigma_\theta^{LA} &= 2.9 \pm 0.6 \text{ mrad}, \\ \sigma_\phi^{LA} &= \frac{2.6 \pm 0.3}{\sin\theta} \text{ mrad}, \end{aligned} \tag{5.13}$$

where errors are determined by fitting the result.

Chapter 6

τ pair selection and decay mode identification

6.1 τ pair event selection

After subtracting non-physics events such as beam-gas events from raw data, τ pair events are selected as follows.

At first it is noteworthy to mention that, at TRISTAN energies, a τ pair event appears as two highly collimated low multiplicity jets in approximately opposite directions(Figure 6.1). As shown in Figure 6.1, an event is separated into two hemispheres by a plane perpendicular to the thrust axis, where the thrust is calculated using all charged particles. Here, thrust T in an event is defined as:

$$T = \max\left(\frac{\sum_{i=1}^{N} |\vec{p}_i \cdot \hat{n}|}{\sum_{i=1}^{N} |\vec{p}_i|}\right), \tag{6.1}$$

where i denotes i-th charged particle and the direction $\hat{n}$ is called "*thrust axis*" *i.e.* the axis along which sum of longitudinal momenta are maximized.

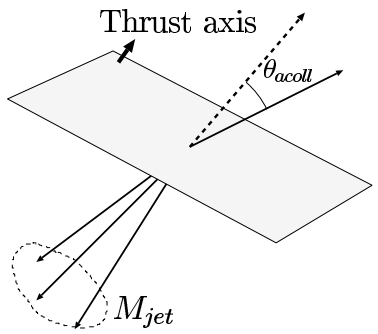

Figure 6.1: Schematic view of a typical τ pair event and definition of jet.

Events which satisfy following requirements are selected as τ pair events.

1 $2 \leq \mathrm{N}_{\text{good track}} \leq 8$, where a "good track" is defined as a track which satisfies,

1-A $|\cos\theta| \leq 0.5$

1-B $N_{\text{axial-hit}} \geq 10$ and $N_{\text{slant-hit}} \geq 4$, where $N_{\text{axial-hit}}(N_{\text{slant-hit}})$ is the number of slant(axial) wire hits which associate to the track.

1-C $|R_{\min}| \leq 2$ cm and $|Z_{\min}| \leq 15$ cm, where $R_{\min}(Z_{\min})$ is the distance at the closest approach between the track and the interaction point as shown in Figure 5.1.

1-D $p_t \geq 0.2$ GeV/c, where p_t is the transverse momentum to the beam axis,

where the requirement **1-A** comes from the most limited acceptance of the muon chamber, **1-B** and **1-C** guarantees high efficiency of track reconstruction in CDC as described in 5.1.1, and **1-D** suppresses the curling tracks in CDC.

2 $\mathrm{N}_{\text{high-}p\text{ track}} \geq 2$, where a high-$p$ track is defined as the "good track" which satisfies following conditions

2-A $p_t \geq 0.7$ GeV/c,

2-B $|\Delta\mathrm{TOF}| \leq 5$ nsec,

where $|\Delta\mathrm{TOF}|$ is defined as the difference of time-of-flight measured by TOF and expectation from the flight length between the interaction point and TOF counter of a track.

3 $(E_{\mathrm{LG}} + E_{\mathrm{LA}})/\sqrt{s} \leq 0.8$, where $E_{\mathrm{LG}}(E_{\mathrm{LA}})$ is total energy deposit in LG(LA).

4 Good tracks in an event must form "1-n" topology, where n=1,3,5,7,

5 $E_{\text{vis}}/\sqrt{s} \geq 0.2$, where E_{vis} is total visible energy of the event *i.e.* $E_{\text{vis}} \equiv E_{\mathrm{LG}} + E_{\mathrm{LA}} + \sum_i |p_i|$($p_i$ denotes the momentum of i-th charged particle),

6 $\theta_{\text{acoll}} < 40^\circ (\cos\theta_{\text{acoll}} \geq 0.766)$, where θ_{acoll} is the acollinearity angle of two jets as shown in Figure 6.1.

7 $M_{\text{jet}} \leq 4.0$ GeV/c^2, where M_{jet} is the jet mass which means the invariant mass of all charged particles in the hemisphere[1] separated by a plane perpendicular to the thrust axis of the event.

[1]When a hemisphere contains only one charged track, $M_{\text{jet}} = 0$ by definition.

The requirement **1** in the selection of τ pair events puts an upper limit on the number of good tracks because the number of charged particles in τ pair event is very low. The requirement **2** assures stable trigger efficiency because the fast track-finder(described in Chapter 4) has the efficiency of more than 99% for tracks which have transverse momenta larger than 0.7 GeV/c *i.e.* for high-p tracks and almost all τ pair events are expected to be triggered by the coplanar trigger or LG segment sum trigger which require two tracks reconstructed by the fast track-finder. Also the requirement **2** reduces cosmic ray events by TOF requirement. The third criterion **3** reduces apparent Bhabha events which deposit all the energies in the electromagnetic calorimeter. In the requirement **4**, "1-n" topology means that one τ decays to one-prong mode such as $e\bar{\nu}\nu$, $\mu\bar{\nu}\nu$ and another τ decays to n-prong mode(n=1,3,5,7)(Figure 6.1). In fact, since the branching fraction of the τ lepton to one-prong mode is about 85 % and that to three-prong mode is about 14 % [13], about 96 % of τ leptons appear in 1-1 or 1-3 topology. n is limited up to 7(*i.e.* $2 \leq N_{\text{good track}} \leq 8$), since at most five charged tracks from τ lepton decay ($\tau^- \to 3h^-2h^+\nu_\tau$ or $\tau^- \to 3h^-2h^+\pi^0\nu_\tau$, h denotes π or K) are observed so far[13].

The requirements **1** and **7** are very effective to reduce multihadronic events whose average multiplicity is about 15 and M_{jet} is large. Figure 6.2(a) and (b) show the $N_{\text{good track}}$ and M_{jet} distribution for τ pair(solid line histogram) and multihadronic(dashed line histogram) Monte Carlo events, respectively. 95.7$\pm$0.2 % of multihadronic events are reduced by these requirements.

The requirements **5** and **6** reduce the two-photon events. Here, a two-photon event means the collision of two virtual photons radiated from the initial e^+ and e^-. Since they are frequently radiated along the beam, the center-of-mass energy of two-photon system is relatively small and the two-photon system is boosted to the beam direction. This is the reason why these cuts are efficient for reduction of such events. Figure 6.3(a) and (b) show the E_{vis} and $\cos\theta_{\text{acoll}}$ distribution for τ pair(solid line histogram) and two-photon(dashed line histogram) Monte Carlo events, respectively. 99.8$\pm$0.6 % of two-photon events are reduced by these requirements.

In the remaining part of this thesis, data sample of events which have passed above τ pair selection is called "τ pair sample".

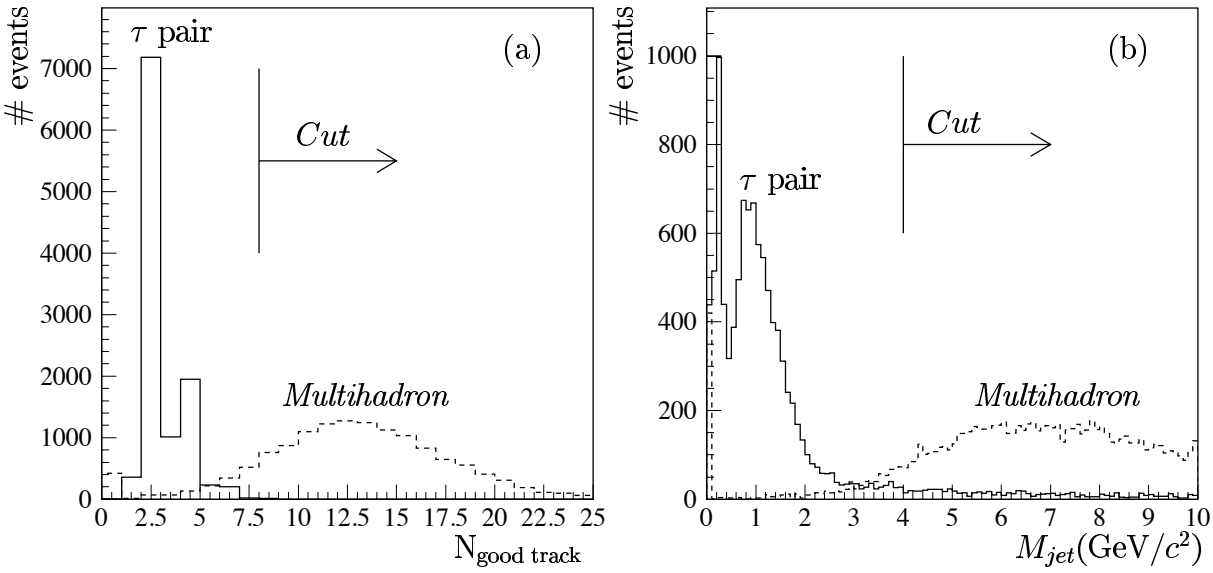

Figure 6.2: (a)$N_{\text{good track}}$ and (b)M_{jet} distribution for τ pair(solid line histogram) and multihadronic(dashed line histogram) Monte Carlo events. The arrows in the figures show the cuts for τ pair selection.

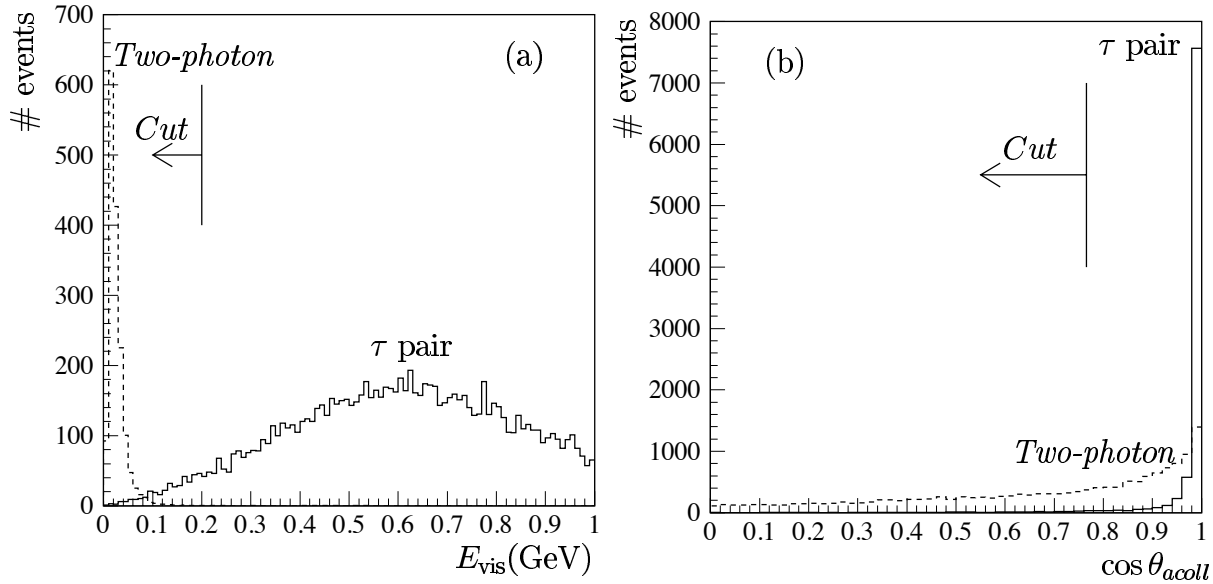

Figure 6.3: (a)E_{vis} and (b)$\cos\theta_{\text{acoll}}$ distribution for τ pair(solid line histogram) and two-photon(dashed line histogram) Monte Carlo events. The arrows in the figures show the cuts for τ pair selection.

Figure 6.4 show a selected typical τ pair event whose topology is 1-3.

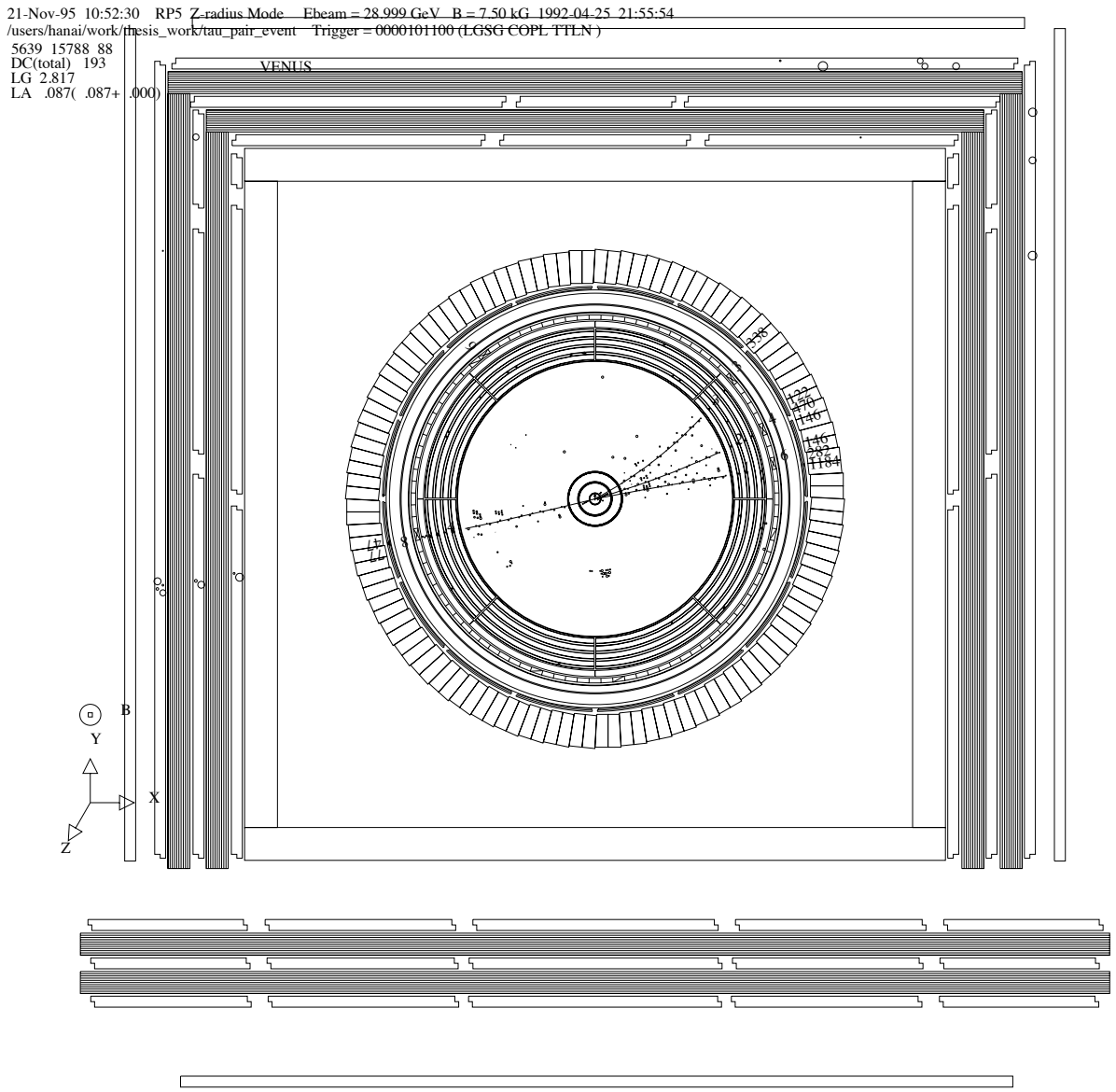

Figure 6.4: typical τ pair event(1-3 topology)

6.2 Decay mode identification

For the study of four different decay modes of $\tau \to e\bar{\nu}\nu, \mu\bar{\nu}\nu, \pi(K)\nu$ and $\rho\nu$, the analysis concentrated to 1-prong hemisphere of 1-n topology in the τ pair sample. The particle identification of the track$(e, \pi(K), \mu, \rho)$ in 1-prong hemisphere is essential for the measurement of τ polarization. Detailed description of the identification of e, $\pi(K)$ and μ is presented in Appendix A.

Detection of the photon is also needed for the identification of ρ meson which is decaying into a pair of charged and neutral pions followed by successive decays into two photons.

Identification of $\tau \to \rho\nu$ mode is described in Section 6.2.1 and identification of $\tau \to e\bar{\nu}\nu$ mode is discussed in Section 6.2.2. Identification of $\tau \to \mu\bar{\nu}\nu$ mode is discussed in Section 6.2.3 and $\tau \to \pi(K)\nu$ mode in Section 6.2.4. Identification of photon is described in Appendix A.

6.2.1 $\tau \to \rho\nu$

Identification of $\tau \to \rho\nu$ mode is performed by identifying ρ meson in 1-prong hemisphere in the τ pair sample. ρ meson is identified by requiring a charged track with accompanying one or two photons in the same hemisphere as described in Appendix A.

In the $\tau \to \rho\nu$ mode, 829 τ's are identified.

6.2.2 $\tau \to e\bar{\nu}\nu$

As described in Appendix A, the identification of $e^{\pm}$ is based on the fact that they deposit their whole energy in LG calorimeter and deposit relatively large energy in TRD.

If a track in the 1-prong hemisphere is identified as an electron in the τ pair sample, it is a candidate of $\tau \to e\bar{\nu}\nu$. Here, 1-1 topology event where both tracks are identified as electrons is discarded because such an event is indistinguishable from Bhabha event.

564 τ's are identified in $\tau \to e\bar{\nu}\nu$ mode.

6.2.3 $\tau \to \mu\bar{\nu}\nu$

As described in Appendix A, μ's are identified using the muon chamber, which is located outside of the iron return yoke.

If a track in the 1-prong hemisphere is identified as μ in the τ pair sample, it is a candidate of $\tau \to \mu\bar{\nu}\nu$. Here, 1-1 topology event where both tracks are identified as μ's is discarded because such an event is indistinguishable from μ pair event.

628 τ's are identified in $\tau \to \mu\bar{\nu}\nu$ mode.

6.2.4 $\tau \to \pi(K)\nu$

As described in Appendix A, π's are identified by using informations from CDC, LG and the muon chamber.

If a track in the 1-prong hemisphere is identified as π in the τ pair sample, it is a candidate of $\tau \to \pi(K)\nu$.

287 τ's are identified in $\tau \to \pi(K)\nu$ mode.

6.3 Efficiency and background

Efficiency of identifying each decay mode is estimated by Monte Carlo data accounting the particle identification efficiencies, which are estimated using the real data, described in Appendix A. They are defined as the ratios of the number of correctly selected decays to the number of generated decays.

There are two kinds of backgrounds in the analysis. One comes from other decay modes than that under study. The other comes from the non τ pair events such as Bhabha, μ pair and two-photon events. Backgrounds of former types can be estimated from the misidentification probability evaluated in Appendix A and the latter is estimated by using the Monte Carlo simulation for various processes with the probability of particle misidentification described in Appendix A.

6.3.1 τ Monte Carlo Data

Monte Carlo data for the process $e^+e^- \to \tau^+\tau^-$are generated by using KORALZ4.0[39] which includes initial and final state bremsstrahlung corrections up to $O(\alpha^2)$ and $O(\alpha)$ electroweak corrections. KORALZ4.0 can produce τ pair events with any value of the τ polarization. Generated events are allowed to decay with the help of TAUOLA2.5[40] which takes into account the τ polarization. Then these events are passed through the VENUS detector with VMONT simulator. The simulated τ events are reconstructed with VENUS standard routine. The same selections as those of real data analysis are applied to the Monte Carlo data.

Total integrated luminosity of Monte Carlo data used in the present analysis is 2,500 pb^{-1}, which is about 10 times larger than the real data.

6.3.2 Identification efficiency of τ decay modes

To obtain the efficiencies, both generated and simulated events are analyzed and the decay tracks of each channels are identified, where "generated" and "simulated" events mean τ pair Monte Carlo events just before and after passing the VENUS detector simulator VMONT, respectively. Since the true assignment of decay modes is known, the number of correctly identified events can be obtained. Dividing this number by that of

generated events the efficiency of each decay mode can be obtained. Evaluated efficiencies are summarized in Table 6.1.

6.3.3 Background from other τ decay modes

The background fraction in each decay mode is obtained by estimating the ratio of the number of wrongly identified decay modes to the number of generated decay modes. The summary of efficiencies and background fractions of each channel are described in Table 6.1.

Decay modes		$\rho\nu$	$\pi(K)\nu$	$e\bar{\nu}\nu$	$\mu\bar{\nu}\nu$
Number of events		829	287	564	628
Efficiency(%)		36.1±1.0	24.3±0.8	34.5±1.0	41.3±1.3
Backgrounds	$\rho\nu$	-	7.8±0.9	1.1±0.3	3.1±0.6
$\tau\tau$ Monte Carlo	$\pi(K)\nu$	67.7±2.6	-	0.6±0.2	3.0±0.6
(events)	$e\bar{\nu}\nu$	2.4±0.5	0.8±0.3	-	< 0.23
	$\mu\bar{\nu}\nu$	0.1±0.1	17.1±1.3	< 0.23	-
	$a_1\nu$	5.2±0.7	0.2±0.1	0.3±0.2	0.1±0.1
	Total	75.6±8.1	25.9±1.6	2.0±0.4	6.2±0.8

Table 6.1: Efficiencies and backgrounds from τ Monte Carlo study. Efficiency in this table is the ratio between the number of correctly identified events to that of generated events in the acceptance($|\cos\theta| < 0.5$ and $\theta_{\rm acoll} < 40^\circ$)

6.3.4 Background from non τ decay process

There are various processes that can be contained in the τ pair sample. Two prong events such as Bhabha or μ pair events, can contaminate the sample due to the misidentification of the particles. For example, if one electron is misidentified as a pion in Bhabha event, this event is considered as

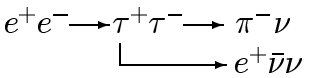

and affects both $\pi(K)\nu$ and $e\bar{\nu}\nu$ mode at the same time.
Such possible background events are described below and estimated number of background events are summarized in Table 6.2.

μ pair events($\mu\mu(\gamma)$)

If one μ fails to be identified correctly in a μ pair event, it can be identified as π or ρ. Thus μ pair events with misidentified μ's can be contained in $\mu\bar{\nu}\nu$, $\pi(K)\nu$ and $\rho\nu$ mode. The probability that μ is misidentified as electron is negligible.

Using 1068.4 pb^{-1} of Monte Carlo data, 6.2 ± 1.0 μ's are identified as $\rho\nu$, 3.1 ± 0.7 as $\pi(K)\nu$ and 15.4 ± 1.2 as $\mu\bar{\nu}\nu$ normalized to the present luminosity.

Hadronic events

Hadronic events can become backgrounds in all τ decay modes because they contain π, μ, electron and photon. Analyzing 357.1 pb^{-1} of Monte Carlo data, 1.1 ± 0.5 tracks are identified as $\pi(K)\nu$, 2.1 ± 1.0 as $\rho\nu$, 2.3 ± 1.2 as $e\bar{\nu}\nu$ and 0.8 ± 0.6 as $\mu\bar{\nu}\nu$ mode normalized to the present luminosity.

Bhabha events($e^+e^-(\gamma)$)

Because an electron may be misidentified as π, Bhabha events can be backgrounds in $e\bar{\nu}\nu$, $\pi(K)\nu$ and $\rho\nu$ mode. The probability that electron is misidentified as μ is negligible.

Since large CPU time is necessary for the full simulation of the electron shower in the calorimeter(LG), only tracking devices are simulated and shower simulation is done by smearing the LG clusters for Bhabha events. Monte Carlo data corresponding to the integrated luminosity of 50 pb^{-1} are examined with the τ selection and it is found that 1.2 ± 0.5 electrons are identified as $\pi(K)\nu$, 6.1 ± 1.4 as $\rho\nu$ and 11.3 ± 3.5 as $e\bar{\nu}\nu$ mode normalized to the present luminosity.

Two-photon events

$e^+e^-e^+e^-$: Total 100 pb^{-1} of Monte Carlo events are examined with the τ selection and 1.1 ± 0.7, 1.4 ± 0.8 and 5.7 ± 1.3 events are found to be misidentified as $\rho\nu$, $\pi(K)\nu$ and $e\bar{\nu}\nu$ mode, respectively.

$e^+e^-\mu^+\mu^-$: Total 100 pb $^{-1}$ of Monte Carlo events are examined with the τ selection and 1.3 ± 0.8, 1.2 ± 0.8 and 4.7 ± 1.2 events are found to be misidentified as $\rho\nu$, $\pi(K)\nu$ and $\mu\bar{\nu}\nu$ mode, respectively.

$e^+e^-\tau^+\tau^-$: Total 90 $^{-1}$ of Monte Carlo events are examined with the τ selection and 0.8 ± 0.7, 0.6 ± 0.6, 0.8 ± 0.8 and 0.7 ± 0.7 events are found to be misidentified as $\rho\nu$, $\pi(K)\nu$, $e\bar{\nu}\nu$ and $\mu\bar{\nu}\nu$ mode, respectively.

e^+e^-qq: 300 pb^{-1} of Monte Carlo events are examined with the τ selection and 0.1 ± 0.09, 0.1 ± 0.1, 0.2 ± 0.2, 0.09 ± 0.09 events are found to be misidentified as $\rho\nu$, $\pi(K)\nu$, $e\bar{\nu}\nu$ and $\mu\bar{\nu}\nu$ mode, respectively.

Other processes	$\rho\nu$	$\pi(K)\nu$	$e\bar{\nu}\nu$	$\mu\bar{\nu}\nu$
$e^+e^-(\gamma)$	6.1 ± 1.4	1.2 ± 0.5	11.3 ± 3.5	-
$\mu^+\mu^-(\gamma)$	6.2 ± 1.0	3.1 ± 0.7	-	15.4 ± 1.2
$q\bar{q}$	2.1 ± 1.0	1.1 ± 0.5	2.3 ± 1.2	0.8 ± 0.6
$e^+e^-e^+e^-$	1.1 ± 0.7	1.4 ± 0.8	5.7 ± 1.3	-
$e^+e^-\mu^+\mu^-$	1.3 ± 0.8	1.2 ± 0.8	-	4.7 ± 1.2
$e^+e^-\tau^+\tau^-$	0.8 ± 0.7	0.6 ± 0.6	0.8 ± 0.8	0.7 ± 0.7
$e^+e^-q\bar{q}$	0.1 ± 0.09	0.1 ± 0.1	0.2 ± 0.2	0.09 ± 0.09
Total	17.7 ± 2.4	8.7 ± 1.6	20.3 ± 4.0	21.7 ± 1.9

Table 6.2: Number of background events normalized to the present luminosity from other process.

6.3.5 Measurement of Branching fraction

Branching fractions of the four decay modes can be estimated by using the following formula,

$$B_i = \frac{N_i \times (1 - f_i^B)}{\epsilon_i \times 2 \times N_{\rm tot}}, \tag{6.2}$$

where B_i is a branching fraction of decay mode $i(i = \rho\nu,\ \pi(K)\nu,\ e\bar{\nu}\nu$ and $\mu\bar{\nu}\nu)$, N_i is the number of candidates in the decay mode i after subtracting the contamination from non-τ background processes, f_i^B is background fraction from other decay modes of τ and ϵ_i is selection efficiency of the mode i. Factor '2' in the denominator means that there are two τ's in an event. $N_{\rm tot}$ is the total number of τ pair events which can be calculated from the measured luminosity as $N_{\rm tot} = \int Ldt \times \sigma_{\rm theory}$, where $\sigma_{\rm theory}$ is the theoretical cross section for τ pair production including radiative corrections in the acceptance($|\cos\theta| < 0.5$ and $\theta_{\rm acoll} < 40^\circ$) and $\int Ldt$ is an integrated luminosity measured by using Bhabha events. In the present analysis, $\sigma_{\rm theory}$ is calculated by KORALZ4.0[39] to be

$$\sigma_{\rm theory} = 15.60 \pm 0.01 \text{ pb} \qquad \text{for } |\cos\theta| < 0.5 \text{ and } \theta_{\rm acoll} < 40^\circ,$$

and $\int Ldt$ is measured by using Bhabha events

$$\int Ldt = 270.8 \pm 5.4 \text{ pb}^{-1}.$$

Using above values, $N_{\rm tot}$ is calculated as

$$N_{\rm tot} = 4224 \pm 84 \text{ events}$$

There are a lot of measurements on the branching fractions of the τ decays from various experiments. Table 6.3 shows the present measurements and comparison with world average values[13]. The measured values agree well with the world average within errors, which confirms that the identification efficiency of τ decay modes is well estimated.

	$\rho\nu$	$\pi(K)\nu$	$e\bar{\nu}\nu$	$\mu\bar{\nu}\nu$
$N_i \times (1 - f_i^B)$	735.7	252.4	541.7	600.1
ϵ_i	36.1±1.0	24.3±0.8	34.5±1.0	41.3±1.3
Branching fraction(%)	24.1±0.9±0.8	12.3±0.8±0.5	18.6±0.8±0.7	17.2±0.7±0.6
PDG94(%)	25.2±0.4	12.4±0.4	18.01±0.18	17.65±0.24

Table 6.3: Branching fractions in τ decays obtained by VENUS detector. The first errors are statistical and the second are systematic ones which originate from uncertainties in efficiencies, luminosity measurement and theoretical cross section.

Chapter 7

Evaluation of the τ polarization and discussion

7.1 Measurement of the τ polarization

As described in Chapter 3, the τ polarization is measured by obtaining the linear combination of the $h = \pm 1$ Monte Carlo data which fits the data best for each τ decay mode. The τ polarization of the background modes is taken to be the same, while fake τ's in non-tau backgrounds are assumed to be unpolarized. So, fitting is done after subtraction of the non-tau backgrounds by minimizing the following χ^2,

$$\chi^2 = \sum_i \left[\frac{N_i^{meas} - \frac{1}{2}[(1+P_\tau)(N_i^+ + N_i^{BG+}) + (1-P_\tau)(N_i^- + N_i^{BG-})]}{\sigma_i} \right]^2 \tag{7.1}$$

where N_i^{meas} is the measured number of real events in bin i after subtraction, of non-tau backgrounds, $N_i^+(N_i^-)$ and $N_i^{BG+}(N_i^{BG-})$ are the numbers of Monte Carlo events in bin i in the correct and wrong decay modes coming from right-(left-)handed τ's. To obtain a polarization asymmetry, fitting is done dividing events into two regions *i.e.* forward region($0 < \cos\theta < 0.5$) and backward region($-0.5 < \cos\theta < 0$).

$e\bar{\nu}\nu$ mode

Figure 7.1 shows the results of fitting for $\tau \to e\bar{\nu}\nu$ mode. Filled circles with error bars show x distribution of electrons from identified $\tau \to e\bar{\nu}\nu$ modes. Solid line histogram shows the fitted linear combination of the Monte Carlo data for the contributions from left-handed(dotted) and right-handed(dashed) τ. Shaded histogram shows the background contribution.

The result from fitting is

$$P_\tau = 0.13 \pm 0.18. \tag{7.2}$$

Tau polarizations in forward and backward region are,

$$P_\tau^F = 0.12 \pm 0.26, \tag{7.3}$$
$$P_\tau^B = 0.13 \pm 0.24.$$

Using these values, polarization asymmetry can be obtained from Eq.(2.12);

$$A_P^{obs} = -0.02 \pm 0.17 \tag{7.4}$$

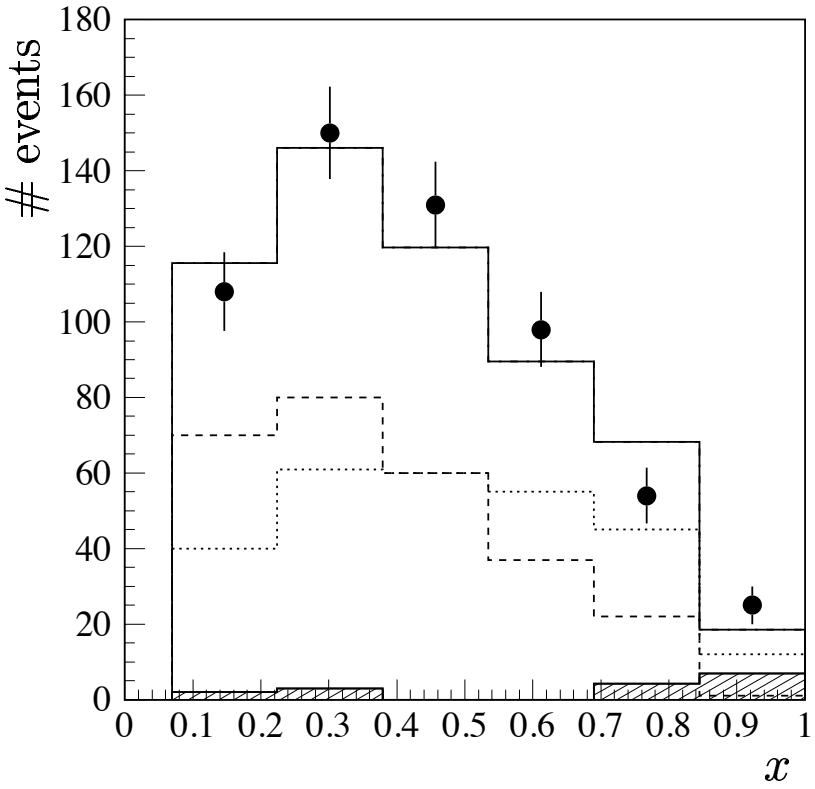

Figure 7.1: x distribution of electrons from $\tau \to e\bar{\nu}\nu$ candidates(filled circles with error bars). Solid line histogram shows the Monte Carlo best fits and dotted(dashed) histogram shows the contribution from left-handed(right-handed) τ.

$\mu\bar{\nu}\nu$ mode

Figure 7.2 shows the results of fitting for $\tau \to \mu\bar{\nu}\nu$ mode.

Result from fitting is

$$P_\tau = 0.15 \pm 0.16. \tag{7.5}$$

Tau polarizations in forward and backward region are,

$$\begin{aligned} P_\tau^F &= 0.17 \pm 0.23, \\ P_\tau^B &= 0.16 \pm 0.21. \end{aligned} \tag{7.6}$$

Using these values, polarization asymmetry can be obtained from Eq.(2.12);

$$A_P^{obs} = -0.01 \pm 0.16 \tag{7.7}$$

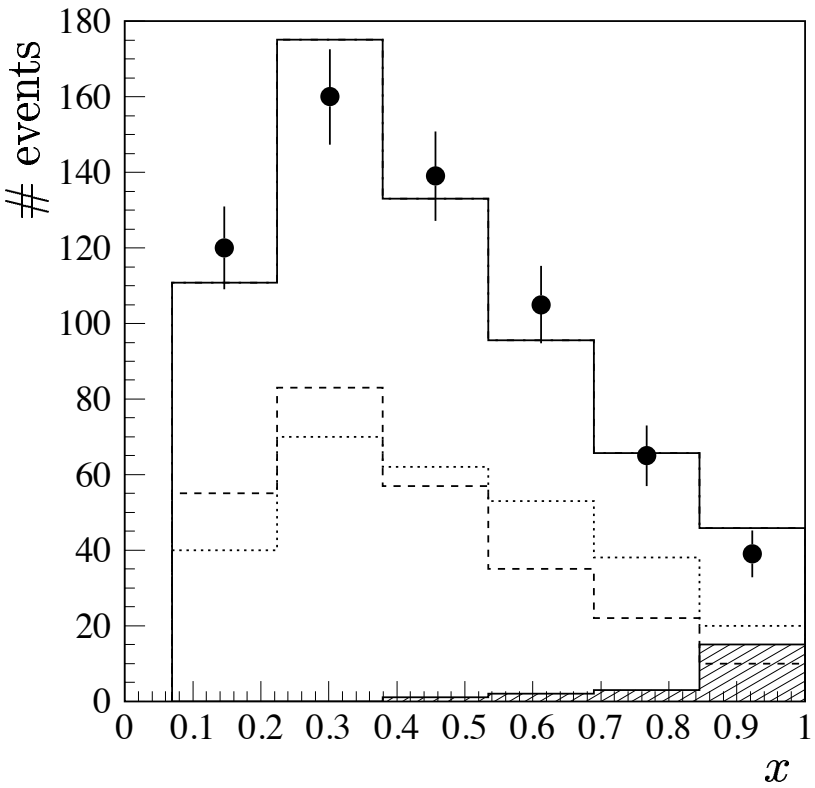

Figure 7.2: x distribution of μ's from $\tau \to \mu\bar{\nu}\nu$ candidates(filled circles with error bars). Solid line histogram shows the Monte Carlo best fits and dotted(dashed) histogram shows the contribution from left-handed(right-handed) τ.

$\pi(K)\nu$ mode

Figure 7.3 shows the results of fitting for $\tau \to \pi(K)\nu$ mode.

Result from fitting is

$$P_\tau = -0.01 \pm 0.12. \tag{7.8}$$

Tau polarizations in forward and backward region are,

$$\begin{aligned} P_\tau^F &= 0.021 \pm 0.17, \\ P_\tau^B &= -0.042 \pm 0.18. \end{aligned} \tag{7.9}$$

Using these values, polarization asymmetry can be obtained from Eq.(2.12);

$$A_P^{obs} = 0.032 \pm 0.12 \tag{7.10}$$

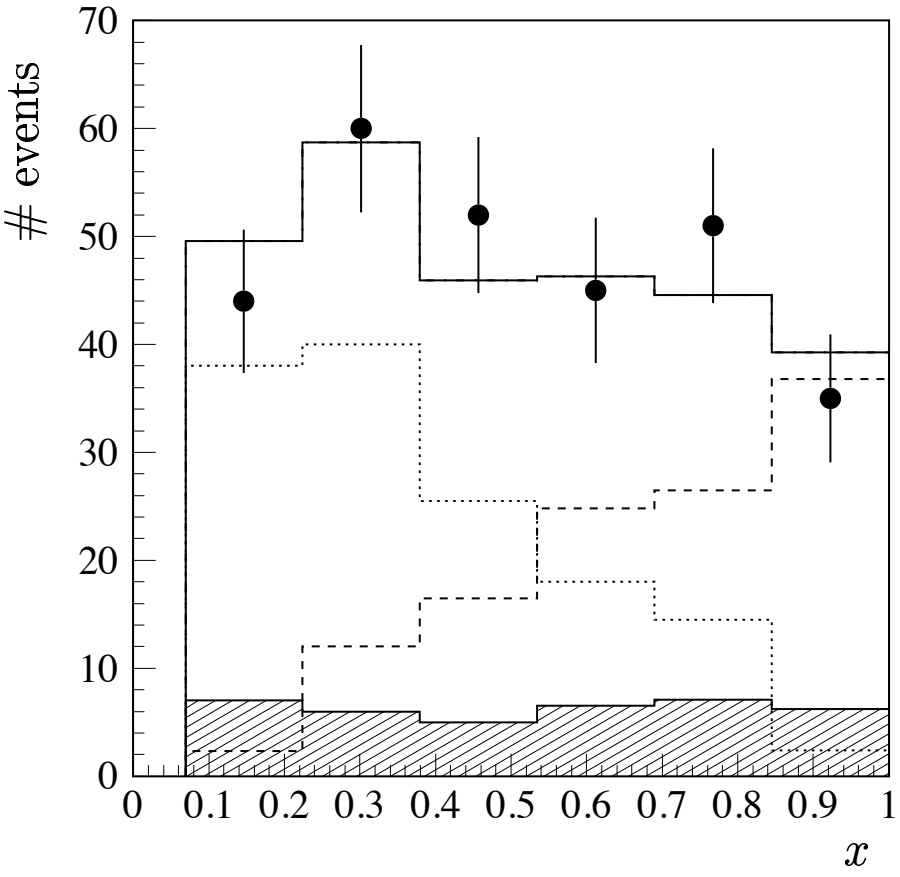

Figure 7.3: x distribution of $\pi(K)$'s from $\tau \to \pi(K)\nu$ candidates(filled circles with error bars). Solid line histogram shows the Monte Carlo best fits and dotted(dashed) histogram shows the contribution from left-handed(right-handed) τ.

$\rho\nu$ channel

As described in Chapter 3, the τ polarization for $\tau \to \rho\nu$ mode is evaluated by measuring the distribution of ψ_ρ in the two ψ_τ regions,

$-1 < \cos\psi_\tau < 0$ and $0 < \cos\psi_\tau < 1$.

Figure 7.4 shows the results of fitting which are performed for two ψ_τ regions simultaneously.

Result from fitting is

$$P_\tau = -0.03 \pm 0.07. \tag{7.11}$$

Tau polarizations in forward and backward region are,

$$P_\tau^F = 0.01 \pm 0.10, \tag{7.12}$$
$$P_\tau^B = -0.07 \pm 0.096.$$

Using these values, polarization asymmetry can be obtained from Eq.(2.12);

$$A_P^{obs} = 0.043 \pm 0.07 \tag{7.13}$$

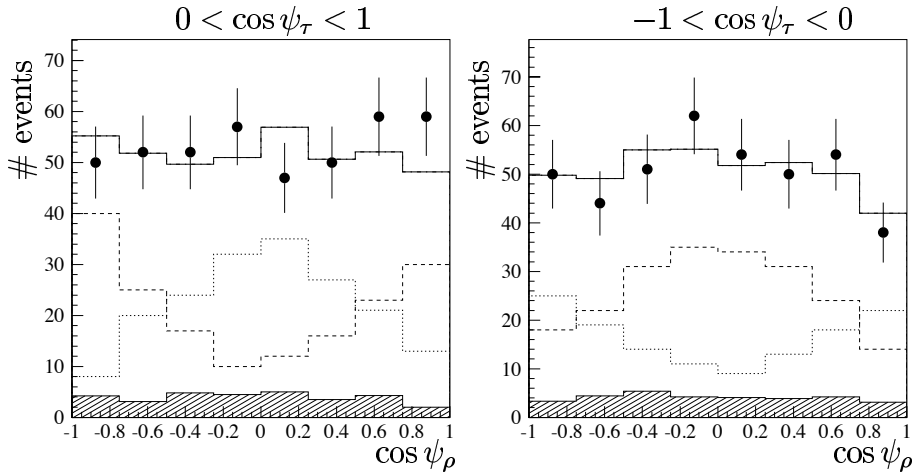

Figure 7.4: $\cos\psi_\rho$ distributions in the region of $0 < \cos\psi_\tau < 1$(left) and $-1 < \cos\psi_\tau < 0$(right) for $\tau \to \rho\nu$ candidates. In each figure, filled circles with error bars shows the data and solid line histogram shows the Monte Carlo best fits and dotted(dashed) histogram shows the contribution from left-handed(right-handed) τ.

7.2 Systematic uncertainties in τ polarization

The source of systematic errors includes, uncertainties in the estimation of efficiencies, background contaminations and Monte Carlo statistics. The former two uncertainties

in the polarization are estimated by varying the efficiency or background contamination within their errors. Last uncertainty is important because it can be change the distribution of the Monte Carlo events.

Error	$e\bar{\nu}\nu$	$\mu\bar{\nu}\nu$	$\pi(K)\nu$	$\rho\nu$
Efficiency	0.021	0.021	0.018	0.024
Tau background	0.014	0.013	0.010	0.009
Non-tau background	0.012	0.008	0.009	0.011
Monte Carlo statistics	0.021	0.020	0.013	0.015
Total systematic error	0.035	0.033	0.026	0.032

Table 7.1: Summary of systematic errors on τ polarization for each decay channel

Error	$e\bar{\nu}\nu$	$\mu\bar{\nu}\nu$	$\pi(K)\nu$	$\rho\nu$
Efficiency	0.023	0.025	0.017	0.026
Tau background	0.015	0.012	0.011	0.009
Non-tau background	0.013	0.008	0.010	0.014
Monte Carlo statistics	0.022	0.019	0.015	0.013
Total systematic error	0.038	0.035	0.027	0.033

Table 7.2: Summary of systematic errors on τ polarization asymmetry for each decay channel

Efficiency Any imperfect modelling of the momentum dependence of the efficiency for identifying τ decay modes can influence the measured polarization by distorting the shape of the observed spectra. This kind of systematic uncertainty can be estimated by changing the values of the efficiencies within their errors.

Changes of the number of entries in each bin of the left and right handed Monte Carlo spectra within the values calculated by using the errors of efficiencies lead to uncertainties in the polarization of 0.021 for $e\nu\bar{\nu}$ mode, 0.021 for $\mu\nu\bar{\nu}$ mode, 0.018 for $\pi(K)\nu$ mode and 0.024 for $\rho\nu$ mode. These are summarized in Table 7.1. Also, uncertainties in the polarization asymmetry are estimated as tabulated in Table 7.2.

Backgrounds Uncertainties in the rate or distribution of background events, either from incorrectly identified τ decays or from non-τ sources, can lead to systematic uncertainty on

the τ polarization. This type of systematic uncertainty can be estimated by changing the background fractions in each bin of the spectra within their errors. Estimated systematic uncertainties are tabulated in Table 7.1 and 7.2.

Monte Carlo statistics Because of limited statistics in Monte Carlo events, the numbers of entries in each bin of the left and right handed Monte Carlo data in the x or ψ_ρ distributions(N_i^+ and N_i^- in Eqs.(7.1)) have uncertainties, which lead to systematic uncertainty on the τ polarization. This type of systematic uncertainty can be estimated by changing N_i^+ and N_i^- in Eqs.(7.1) for each fit within their statistical uncertainties. Estimated systematic errors tabulated in Table 7.1 and 7.2.

7.3 Combined results on τ polarization

Measured τ polarizations for each decay mode are,

$$\begin{aligned}
\mathcal{P}_\tau &= 0.13 \pm 0.18 \pm 0.035 && e\bar{\nu}\nu \text{ mode,} \\
&= 0.15 \pm 0.16 \pm 0.033 && \mu\bar{\nu}\nu \text{ mode,} \\
&= -0.01 \pm 0.12 \pm 0.026 && \pi(K)\nu \text{ mode,} \\
&= -0.03 \pm 0.07 \pm 0.032 && \rho\nu \text{ mode.}
\end{aligned}$$

Combining these results in a weighted average, average tau polarization,

$$P_\tau = 0.012 \pm 0.058$$

is obtained.

Similarly, measured τ polarization asymmetry for each decay mode are,

$$\begin{aligned}
A_\mathcal{P} &= -0.02 \pm 0.17 \pm 0.038 && e\bar{\nu}\nu \text{ mode,} \\
&= -0.01 \pm 0.16 \pm 0.035 && \mu\bar{\nu}\nu \text{ mode,} \\
&= 0.032 \pm 0.12 \pm 0.027 && \pi(K)\nu \text{ mode,} \\
&= 0.047 \pm 0.07 \pm 0.033 && \rho\nu \text{ mode.}
\end{aligned}$$

These are combined to be,

$$A_P^{obs} = 0.029 \pm 0.057.$$

Both statistical and systematic errors are included in above results.

7.4 Discussions on the results

As described in Chapter 2, it is very important to confirm the framework of the Standard Model with $\mathcal{P}_\tau$ and $A_\mathcal{P}$ measurement in the energy region below Z^0 pole, where there is no substantial measurement: the previous measurements have very large errors due to poor statistics. Our results on $\mathcal{P}_\tau$ and $A_\mathcal{P}$ can be compared with those values measured by them below Z^0 pole:MAC[2], CELLO[3] and AMY[4], as shown in Figure 7.5.

The results have relatively small errors thanks to large number of events collected at TRISTAN. Furthermore, the magnitude of the interference term is expected to be six or four times larger in the TRISTAN energy region than the PEP or PETRA energy region, respectively. This implies that the present measurement is more sensitive to the possible anomaly arising from the interference term.

Besides our statistical advantage, the present analysis has several superiorities:

- Excellent particle identification by the TRD: Good separation between electron and π, reduction of misidentification of electron as ρ and vice versa are accomplished. This is the first time that the TRD is used to positively identify π or ρ in e^+e^- annihilation experiments.

- Reliable evaluation of the identification efficiencies and the background contaminations of τ decay modes: The detector response is thoroughly investigated by the real data as described in Appendix A and implemented in the Monte Carlo simulation.

- Rigorous treatment in the radiative corrections: The results are relatively insensitive to the imperfect modelling of the radiative corrections, while in the previous experiments the results are sensitive to that as described in Section 3.3.

Thus, our results are the first substantial measurements of the τ polarization and its forward-backward asymmetry in the energy region below Z^0 pole. As shown in Figures 7.5, they agree well with the expectation of the Standard Model and confirm its framework.

As described in Chapter 2, in Eqs.(2.5), the terms which are important in the energy region below Z^0 pole are different from those in the energy region around Z^0 pole. Therefore, the present results will contribute to test the Standard Model as well as those from LEP.

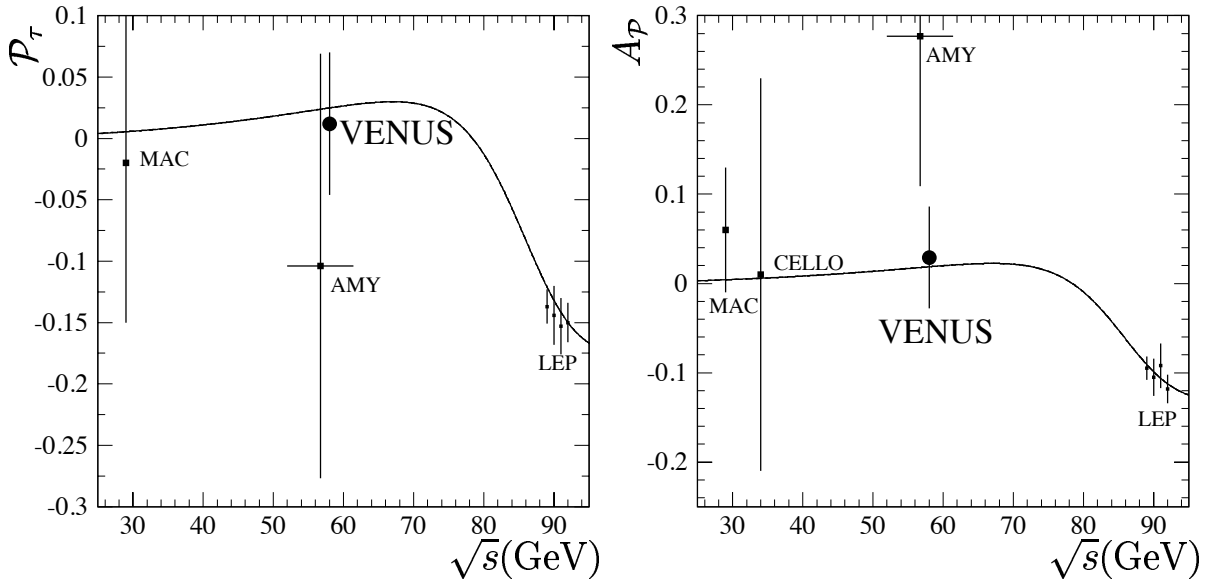

Figure 7.5: Measured values of $\mathcal{P}_\tau$ and $A_\mathcal{P}$ with those from other experiments. Solid line shows the Standard Model expectation.

Within the Standard Model framework, the present results can be interpreted using Eq.(2.12) to the vector coupling constants of electron and τ to Z^0 as,

$$g_V^e = -0.03 \pm 0.07$$
$$g_V^\tau = -0.08 \pm 0.17.$$

These values are plotted with those values of previous experiments evaluated from the τ polarization measurements in Figure 7.6 and they are also the first substantial measurements in the e^+e^- annihilation experiments in the energy region below Z^0 pole.

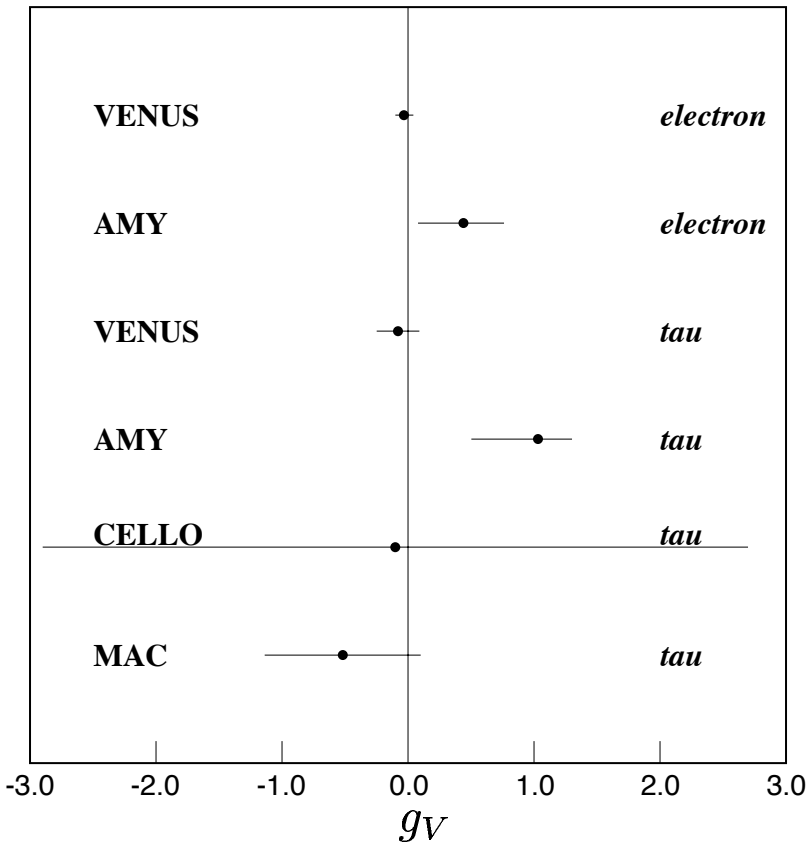

Figure 7.6: Measured values of vector coupling constants of τ and electron in VENUS with those of previous experiments evaluated from the τ polarization measurements. It is not possible to evaluate the value of g_V from only the τ polarization measurement at LEP. The Standard Model expectation of g_V is -0.037$\pm$0.001[13].

Both the measured values of g_V^e and g_V^τ are consistent with the Standard Model expectation($g_V = -0.037 \pm 0.001$[13]). A fundamental prediction of the Standard Model is that the fundamental constant, g, is the same for all leptons as well as α and $\sin^2\theta_W$. This prediction is called 'lepton universality' and has been tested experimentally at various experiments[41] in both charged and neutral current sector. In the charged current sector, it has been tested by measuring the W decays, $W \to l\bar{\nu}_l (l = e, \mu, \tau)$, by measuring the τ decays, $\tau \to l\bar{\nu}_l\nu_\tau (l = e, \mu)$ and by measuring the π decays, $\pi \to l\bar{\nu}_l (l = e, \mu)$. On the other hand, in the neutral current sector, it has been tested by measuring the Z decay asymmetries(forward-backward, τ polarization, left-right). So far the lepton universality is confirmed with the precision better than 0.1 % in the charged current sector[41] and with the precision better than 1 % in the neutral current sector[5, 41]. The present results on g_V^e and g_V^τ can be used to test the e-τ universality at the TRISTAN energy. They are

consistent with the Standard Model value and their ratio is calculated as,

$$\frac{g_V^e}{g_V^\tau} = 0.38 \pm 0.88,$$

which is consistent with unity. It can be said that the present results support the lepton universality.

Furthermore, assuming the lepton universality, g_V^e and g_V^τ should be equal. The vector coupling constant of lepton to Z^0 is obtained by averaging above results on g_V^e and g_V^τ as

$$g_V = -0.037 \pm 0.06,$$

As shown in Table 2.3, g_V is expressed in terms of $\sin^2\theta_W$ as,

$$g_V = -\frac{1}{2} + 2\sin^2\theta_W.$$

The present measurement of g_V corresponds to,

$$\sin^2\theta_W = 0.23 \pm 0.03.$$

This is also the first $\sin^2\theta_W$ measurement at TRISTAN.

Chapter 8

Conclusions

The τ polarization for $e^+e^- \to \tau^+\tau^-$process is studied in the VENUS experiment with the integrated luminosity of 271 pb^{-1} at the center-of-mass energy 58 GeV using the τ decays to $\rho\nu, \pi(K)\nu, e\bar{\nu}\nu$ and $\mu\bar{\nu}\nu$. Branching fractions of the these four decay modes are also measured and found to be consistent with world average values within errors.

Average τ polarization and its forward-backward asymmetry are measured to be,

$$\mathcal{P}_\tau = 0.012 \pm 0.058,$$
$$A_\mathcal{P} = 0.029 \pm 0.057.$$

These values are the first substantial measurements on $\mathcal{P}_\tau$ and $A_\mathcal{P}$ in the energy region below Z^0 pole. It is found that they confirm well the framework of the Standard Model.

Vector coupling constants of τ and electron to electroweak interaction are evaluated from the average τ polarization and its forward-backward asymmetry as

$$g_V^e = -0.03 \pm 0.07,$$
$$g_V^\tau = -0.08 \pm 0.17.$$

These values are more accurate than those of the previous e^+e^- annihilation experiments (CELLO[3], MAC[2] and AMY[4]) and the first substantial measurements in the energy region below Z^0 pole. They also support the lepton universality in the TRISTAN energy region.

From these values of g_V^e and g_V^τ, $\sin^2\theta_W$ are also derived as,

$$\sin^2\theta_W = 0.23 \pm 0.03,$$

assuming the lepton universality. This is the first measurement of substantial value of $\sin^2\theta_W$ at TRISTAN energy($\sqrt{s} = 58$ GeV) and consistent with the most recent value of $\sin^2\theta_W^{eff} = 0.232 \pm 0.001$[13] which is mainly determined by the experiments on Z^0 pole.

Appendix A

Particle identification

A.1 Electron identification

The identification of electron is based on the fact that they deposit their whole energy in LG calorimeter and deposit relatively large energy in TRD. The informations from CDC, LG and TRD are used to identify electron.

E/p Cut based on LG and CDC

E/p is a ratio of energy deposit E[GeV] in the electromagnetic calorimeter LG and momentum p[GeV/c] of an associated charged particle. An electron deposits its all energy in electromagnetic calorimeter where the electromagnetic shower spreads typically over 2×2 blocks. If a track has E/p greater than 0.8, such a track is considered as a candidate of an electron. Here, E is the maximum sum of energy deposit in four LG blocks including the block which is hit by the CDC track and p is the momentum of the track measured by CDC. Figure A.1 shows the E/p distribution for π and electron using π's from $\tau \to 3\pi\nu$ in τ pair events, $K_s \to \pi\pi$ in multihadronic events and $ee\pi\pi$ in two photon events and electrons from Bhabha events.

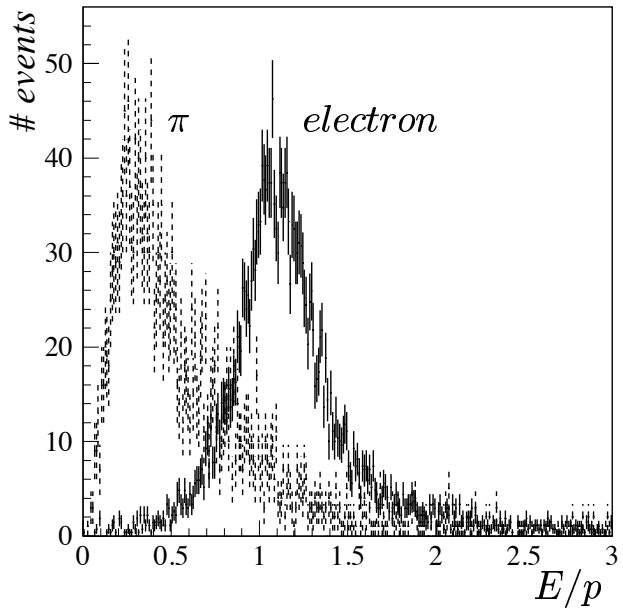

Figure A.1: Energy deposit in LG of π and electron.

$E_{\rm TRD}$ Cut

In addition to above E/p cut, the electron candidate is required to have energy deposit in TRD greater than 10 keV($E_{\rm TRD} \geq$ 10keV). This requirement is to reduce the contamination of other τ decay because ρ meson or radiative τ decay ($\tau \to \mu\bar{\nu}\nu\gamma, \pi\nu\gamma$) may be an electron candidate if the charged particle and photon are merged in one LG cluster where E/p may be unity(Figure A.2).

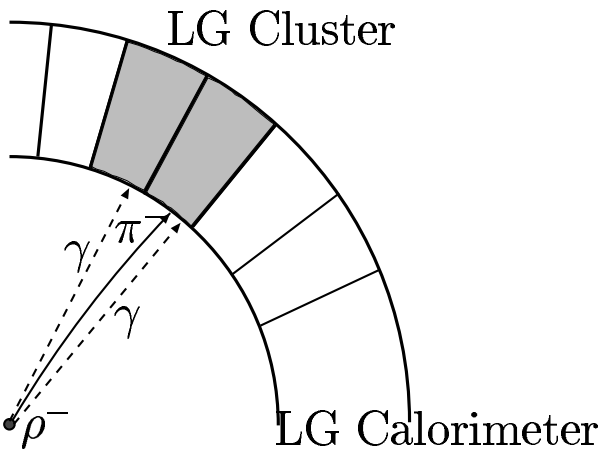

Figure A.2: charged pion and two photons from rho decay are merged

Figure A.3 shows the distribution of the energy deposit in TRD for μ and electron using μ pair events and Bhabha events, respectively. Since transition radiation depends only

on the mass of the traversing charged particle(Eq. 4.5) and the mass difference between μ and π is small, μ is expected to behave like π in TRD.

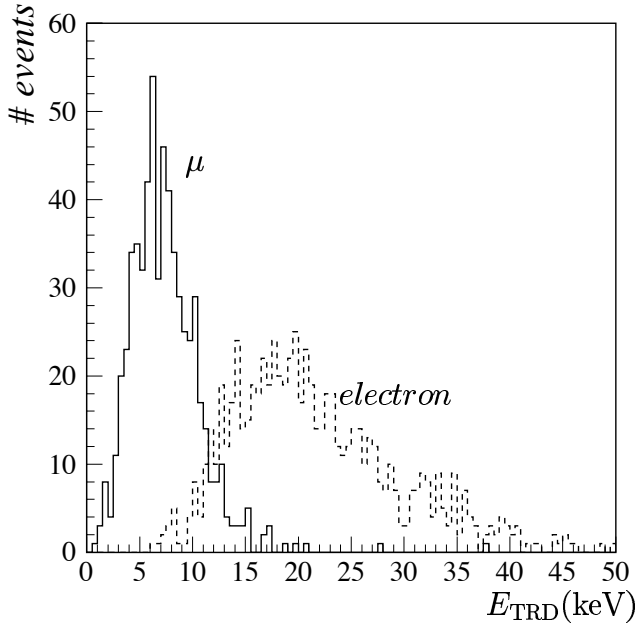

Figure A.3: The distribution of energy deposit in TRD for muon and electron

Efficiency of electron identification

Efficiency of electron identification is evaluated over whole momentum region by using the electron sample from radiative Bhabha($e^+e^- \to e^+e^-(\gamma)$) events which contain electrons of various momentum. The background contamination by E/p cut can be studied by using the π sample from multihadronic events in which the π candidate is required to have the energy deposit in TRD to be less than 8 keV. The background contamination by E_{TRD} cut can be studied by using the μ sample from μ pair and cosmic ray events because the behavior of μ in TRD can be considered to be the same as π as described in Chapter 4. Figure A.4 shows the efficiency of the electron identification as a function of electron momentum. The misidentification efficiency of π is also shown in the figure.

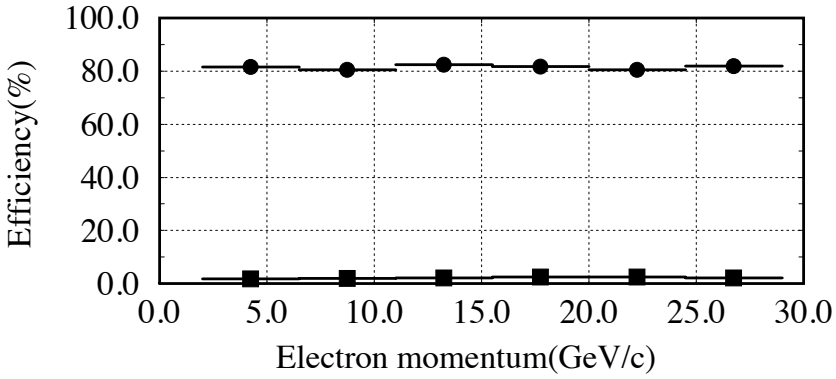

Figure A.4: The electron identification efficiency(filled circles with errors) as a function of momentum evaluated by using electron sample from Bhabha events. Also shown is the probabilities that π is misidentified as electron(filled squares with errors) evaluated by using π sample from $\tau \to 3\pi\nu$, $K_s \to \pi\pi$ and $ee\pi\pi$.

A.2 μ identification

μ identification is performed by using informations from CDC and muon chamber, which is located outside of iron return yoke as described in Chapter 4. In the barrel region, the main absorbing material consists of the lead glasses, their support rings made of 17.5 cm thick iron and 10.0 cm thick aluminum, the return yoke made of 30.0 cm thick iron and two muon filters, each comprising 20.0 cm thick iron. Thickness of each muon filter is chosen to be about one absorption length of hadrons. Since particles should penetrate at least 5.3 absorption length of material up to the second muon filter, most of hadrons and electrons interact in the material and they cannot reach the muon chambers whereas μ's do not interact much in the material.

A CDC track which is associated with at least four hit layers in muon chamber is a μ candidate. Here, "*association*" is determined as follows.

At first, a CDC track is extrapolated to the muon chamber and a certain window is set at each layer of the muon chamber along the extrapolated track. The window is calculated by using the momentum of the track and the thickness of the material through which the track is expected to penetrate to take into account the effect of deflection of the track by the multiple Coulomb scattering. Next, hits in the muon chamber are searched around the extrapolated track and a hit in muon chamber is determined to be "associated with the track" if it exists within $\pm 3\sigma$ around the track.

Figure A.5 shows the schematic view of the extrapolation of CDC track and association of muon chamber hits.

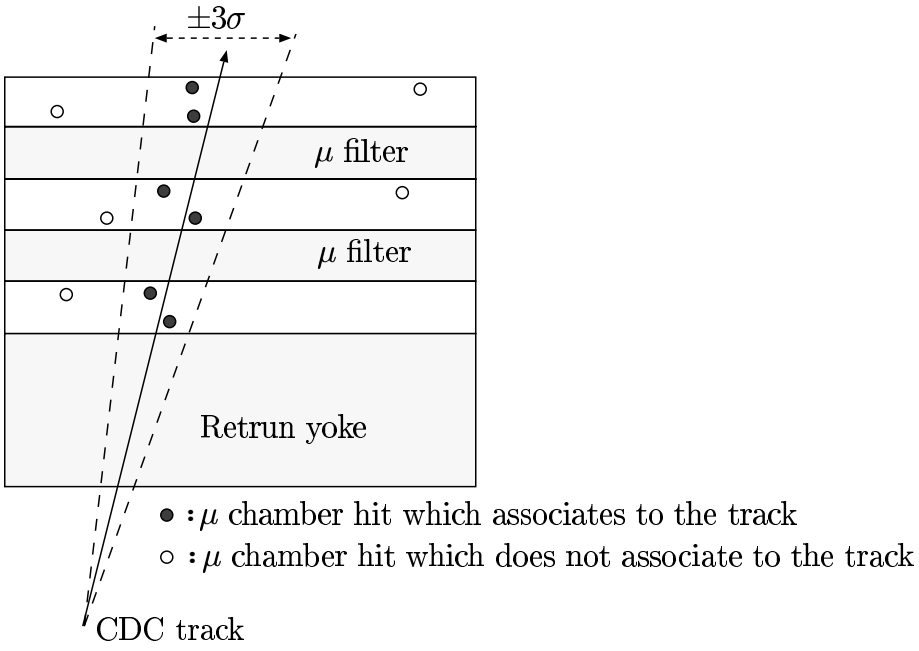

Figure A.5: Schematic view of extrapolated CDC track and muon chamber hits.

Particles which can contaminate μ candidates are π's which may penetrate the material or decay into $\mu\nu_\mu$ in flight. Such a background contamination can be studied by using π's from $\tau \to \rho\nu, 3\pi\nu$, $K_s \to \pi\pi$ in multihadronic events and $ee\pi\pi$ events. Figure A.6 shows background contamination from π as well as the efficiency of μ identification which is measured by using μ sample from μ pair and cosmic ray events.

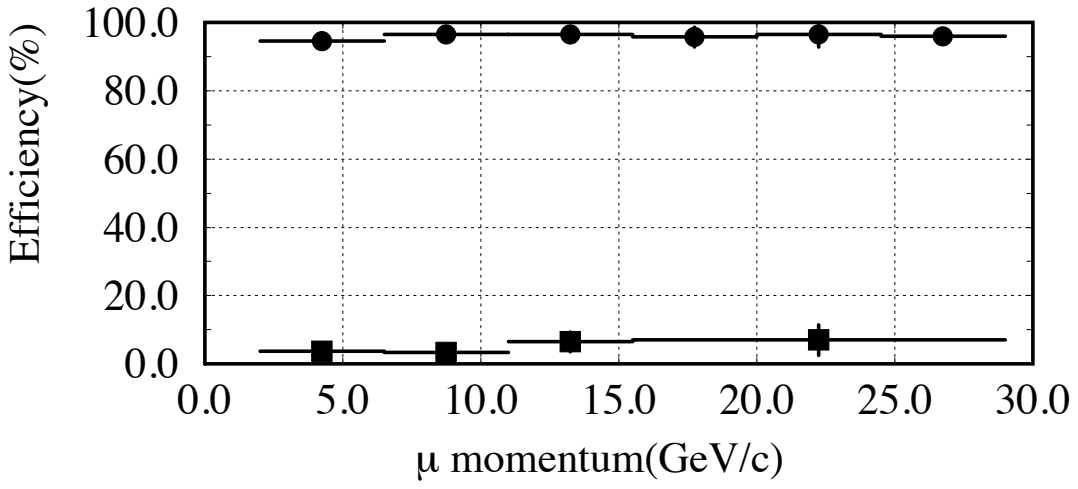

Figure A.6: The μ identification efficiency(filled circles with errors) evaluated by using μ sample from μ pair and cosmic ray events. Also shown is the probability that π is misidentified as μ(filled squares with errors) evaluated by using π sample from $\tau \to \rho\nu, 3\pi\nu$, $K_s \to \pi\pi$ in multihadronic events and $ee\pi\pi$ events.

A.3 $\pi(K)$ identification

The charged track which is neither identified as electron nor μ is a candidate of π or K if there is no neutral clusters with energy higher than 200 MeV within 60°. Separation of π and K is not possible with VENUS detector and they are treated as "π candidates". To reduce the contamination of electron, the π candidate is required to satisfy E_{TRD} <10 keV. The reduction of μ contamination is accomplished by requiring that there should not be more than one associated hits in the muon chamber. Figure A.7 shows the efficiency of pion using $\tau \to 3\pi$ and $\tau \to \rho$ events.

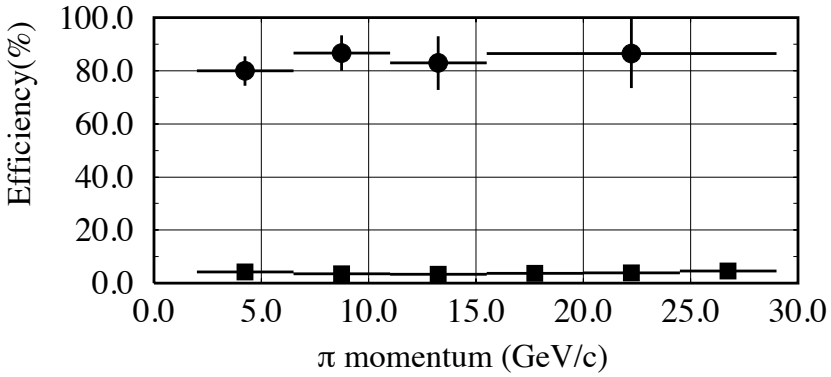

Figure A.7: The π identification efficiency(filled circle with errors). Also shown is the probability that μ is misidentified as π(filled squares with errors). π and μ sample are the same as those used in the previous section.

A.4 ρ identification

ρ meson is identified by requiring a charged track with accompanying one or two photons in the same hemisphere because it decays into a charged and a neutral pion which decays immediately into two photons. The charged track is required to satisfy the π-identification criteria described in the previous section. Higher photon multiplicities are not accepted in order to reduce background from a_1 decays and other multi-hadronic decays. Here a photon is identified as a neutral cluster in the LG calorimeter whose energy is larger than 200 MeV. A "neutral cluster" is the LG cluster which does not match any charged track in CDC.

Two photons from π^0 are frequently merged into a single neutral cluster in the LG because their opening angle is occasionally smaller than the lateral segmentation of the LG for energetic π^0. Also a minimal opening angle of 4° between the charged particle and

any photon is required to reduce background due to shower fluctuations from hadronic interactions of the charged particle in the calorimeter.

Candidate π^0's were subdivided in two different classes:

1. Two neutral clusters of which invariant mass lies within 35 MeV/c^2 around the π^0 mass. Figure A.8(a) shows the invariant mass distribution of two photon candidates.

2. One neutral cluster with energy greater than 1 GeV.

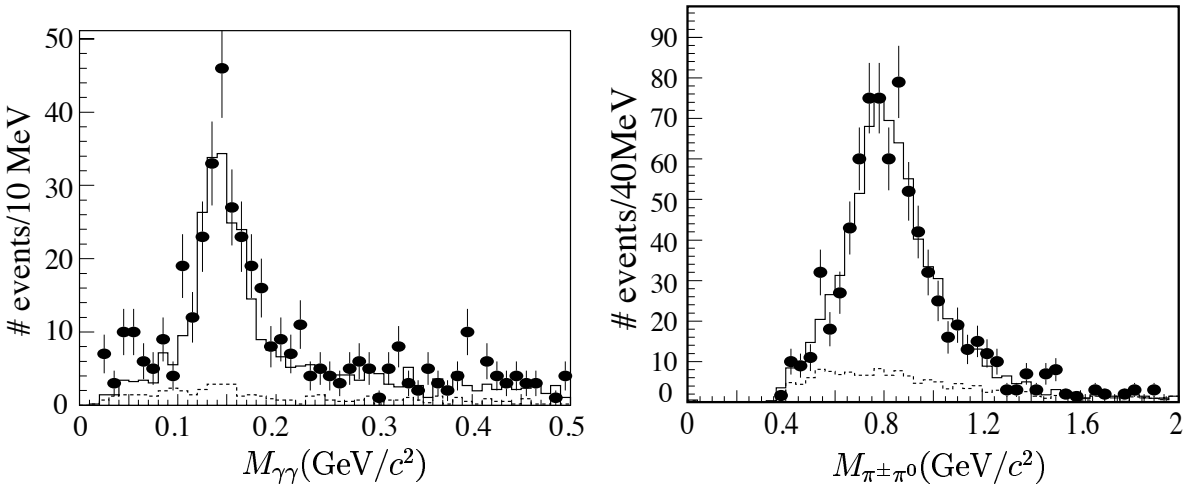

Figure A.8: Invariant mass distribution of (a)two photons and (b)one charged track and π^0 candidate. Filled circle with error bars shows real data from τ pair sample and solid histogram shows Monte Carlo data normalized with luminosity and dashed histogram shows a background from other τ decays and other processes.

The invariant mass distribution of the charged π and the π^0 candidate is shown in Figure A.8(b). In calculation of the invariant mass, $\pi^\pm$ mass is assigned to the charged track and π^0 mass is assigned to the one photon. Particles in a hemisphere which satisfy the condition that the reconstructed invariant mass lyies within $\pm$230 MeV/c^2 around the $\rho^\pm$ mass(770 MeV/c^2) are identified as coming from the ρ meson. Here, the hemisphere in which the track passes the muon selection is discarded to reduce the contamination of muon from radiative μ pair($\mu\mu\gamma$) events or μ from tau decays with radiation($\tau \to \mu\bar{\nu}\nu\gamma$).

Bibliography

[1] H.D.Dahmen, L.Schülke and G.Zech, Phys. Lett. **81B**(1979)361; Z. Phys. **C5**(1980)71;
G.Goggi, Proc. of LEP Summer Study, CERN 79-01 (1979)483;
S.Jadach and Z.Was, Z Physics at LEP 1, Volume 1, CERN 89-08(1989)235.

[2] MAC Collaboration, W.T.Ford *et al.*, Phys. Rev. **D36**(1987)1971.

[3] CELLO Collaboration, H.J.Behrend *et al.*, Phys. Lett. **127B**(1983)270.

[4] AMY Collaboration, M.H.Lee *et al.*, KEK Preprint 90-70(1990).

[5] A.Kounine, Nucl. Phys. B **40** "*Proceedings of the Third Workshop on Tau Lepton Physics*"(1995)437.

[6] M.Kobayashi and K.Maskawa, Progr. Theor. Phys. **49**(1973)652.

[7] S.L.Glashow, Nucl. Phys. **22**(1961)579;
S.Weinberg, Phys. Rev. Lett. **19**(1967)1264;
A.Salam and J.C.Ward, Phys. Lett. **13**(1964)168.

[8] P.W.Higgs, Phys. Lett. **12**(1964)132;
P.W.Higgs, Phys. Rev. Lett. **13**(1964)508;
P.W.Higgs, Phys. Rev. **145**(1966)1156.

[9] F.J.Hasert *et al.*, Phys. Lett. **46B**(1973)138;
F.J.Hasert *et al.*, Nucl. Phys. **B73**(1974)1.

[10] UA1 Collab., Phys. Lett. **B129**(1983)273;
UA2 Collab., Phys. Lett. **B129**(1983)130.

[11] G.Goggi, Proc. LEP Summer Study, Les Houches and CERN(1978), CERN report 79-01(1979) Vol.2 483.

[12] Y.S.Tsai, Phys. Rev. **D4**(1971)2821.

[13] Particle Data Group, Phys. Rev. **D50**(1994).

[14] K. Hagiwara, A.D.Martin and D.Zeppenfeld, Phys. Lett. **B235**(1990)198.

[15] A. Rougé, Z. Phys. **C8**(1990)75.

[16] ALEPH Collaboration, CERN-PPE-95-023, Mar 1995.

[17] DELPHI Collaboration, P.Abreu *et al.*, Z. Phys. **C67**(1995)183.

[18] OPAL Collaboration, R. Akers *et al.*, Z. Phys. **C65**(1995)1.

[19] L3 Collaboration, M. Acciarri *et al.*, Phys. Lett. **341**(1994)245.

[20] TRISTAN Project Group, "*TRISTAN Electron-Positron Colliding Beam Project*," KEK Report 86-14 (1987).

[21] VENUS Collab., KEK Report TRISTAN-EXP-001(1983).

[22] M.Sakuda *et al.*, Nucl. Instr. and Meth. **A311**(1992)57.
N.Kanda "Study of Multihadronic Events Using Decay Electrons," Osaka Univ. (1993) Doctral thesis.

[23] Y.Yamada *et al.*, Nucl. Instr. and Meth. **A330**(1993)64.

[24] R.Arai *et al.*, Nucl. Instr. and Meth. **A217**(1983)181.

[25] T.Ohsugi *et al.*, Nucl. Instr. and Meth. **A269**(1988)522-526.

[26] K.Ogawa *et al.*, Nucl. Instr. and Meth. **A243**(1986)58;
K.Ogawa *et al.*, Nucl. Instr. and Meth. **A271**(1988)432.

[27] Y.Henmi *et al.*, Japan. Jour. of Appl. Phys. **26**(1987)982.

[28] Y.Asano *et al.*, Nucl. Instr. and Meth. **A254**(1987)35;
Y.Asano *et al.*, Nucl. Instr. and Meth. **A259**(1987)430;
Y.Ikegami *et al.*, IEEE Trans. Nucl. Sci. **36**(1989)665.

[29] Y.Fukushima *et al.*, IEEE Trans. Nucl. Sci. **36**(1989)670.

[30] R.Arai *et al.*, Nucl. Instr. and Meth. **254**(1987)317.

[31] T.Umebayashi *et al.*, Nucl. Instr. and Meth. **A265**(1988)457.

[32] H.Saito *et al.*, Nucl. Instr. and Meth. **A270**(1988)319.

[33] F.Takasaki *et al.*, Nucl. Instr. and Meth. **A322**(1992)211.

[34] T.Ohsugi *et al.*, Nucl. Instr. and Meth. **A269**(1988)522.

[35] K.Amako *et al.*, Nucl. Instr. and Meth. **A272**(1988)687.

[36] Y,Nakagawa *et al.*, Japan. Jour. of Appl. Phys. **25**(1986)1049

[37] W.R.Nelson, H.Hirayama and D.W.O.Rogers, "The EGS4 Code System," SLAC-265, Stanford Linear Accelerator Center(1985).

[38] G.A.Akopdjanov *et al.*, Nucl. Instr. and Meth. **140**(1977)441.

[39] S.Jadach, B.F.L.Ward, Z.Was, Comp. Phys. Commun. **79**(1994)503.

[40] S.Jadach, Z.Was, R.Decker, J.H.Kuhn, Comp. Phys. Commun. **76**(1993)361.

[41] W.J.Marciano, Nucl. Phys. B **40** "*Proceedings of the Third Workshop on Tau Lepton Physics*"(1995)3.